

Charge structure and lightning sensitivity in a simulated multicell thunderstorm

Edward R. Mansell¹

Cooperative Institute for Mesoscale Meteorological Studies (CIMMS), University of Oklahoma, Norman, Oklahoma, USA

Donald R. MacGorman and Conrad L. Ziegler

National Severe Storms Laboratory, Norman, Oklahoma, USA

Jerry M. Straka

School of Meteorology, University of Oklahoma, Norman, Oklahoma, USA

Received 27 July 2004; revised 7 March 2005; accepted 23 March 2005; published 17 June 2005.

[1] A three-dimensional dynamic cloud model is used to investigate electrification of the full life cycle of an idealized continental multicell storm. Five laboratory-based parameterizations of noninductive graupel-ice charge separation are compared. Inductive (i.e., electric field-dependent) charge separation is tested for rebounding graupel-droplet collisions. Each noninductive graupel-ice parameterization is combined with variations in the effectiveness of inductive charging (off, moderate, and strong) and in the minimum ice crystal concentration (10 or 50 L⁻¹). Small atmospheric ion processes such as hydrometeor attachment and point discharge at the ground are treated explicitly. Three of the noninductive schemes readily produced a normal polarity charge structure, consisting of a main negative charge region with an upper main positive charge region and a lower positive charge region. Negative polarity cloud-to-ground (CG) flashes occurred when the lower positive charge (LPC) region had sufficient charge density to cause high electric fields. Two of the three also produced one or more +CG flashes. The other two noninductive charging schemes, which are dependent on the graupel rime accretion rate, tended to produce an initially inverted polarity charge structure and +CG flashes. The model results suggest that inductive graupel-droplet charge separation could play a role in the development of lower charge regions. Noninductive charging, on the other hand, was also found to be capable of producing strong lower charge regions in the tests with a minimum ice crystal concentration of 50 L⁻¹.

Citation: Mansell, E. R., D. R. MacGorman, C. L. Ziegler, and J. M. Straka (2005), Charge structure and lightning sensitivity in a simulated multicell thunderstorm, *J. Geophys. Res.*, 110, D12101, doi:10.1029/2004JD005287.

1. Introduction

[2] Numerical modeling of storm electrification is highly dependent on parameterizations of mechanisms by which hydrometeors acquire charge. Laboratory studies [e.g., Reynolds *et al.*, 1957; Takahashi, 1978; Jayaratne *et al.*, 1983; Saunders *et al.*, 1991; Saunders and Peck, 1998] have confirmed that rebounding collisions between small and large ice particles can result in an appreciable separation of charge. This process is referred to as noninductive (i.e., independent of external electric fields) collisional charge separation. The sign and magnitude of the charge gained by the larger particle appears to be dependent on multiple variables; studies have identified temperature, cloud water content, rime accretion rate, and the droplet size spectrum as

factors. The complexity is further compounded by disagreements in the details of the laboratory results.

[3] Only a few studies have employed multidimensional dynamical simulation models with predicted ice-phase microphysics. Rawlins [1982] used a three-dimensional model with “bulk” category microphysics (cloud water, rain, ice crystals, and hail) to examine basic electrical structure of a winter maritime storm. An axisymmetric model with explicit (i.e., bin model) microphysics was used by Takahashi [1984]. Takahashi’s model incorporated laboratory results for charging due to ice rebounding particle collisions [Takahashi, 1978]. His model also included small and large ion categories and ion attachment to hydrometeors. Takahashi [1984] compared maritime to continental storms by varying the concentrations of cloud condensation nuclei and cloud ice nuclei. He concluded that charging due to rebounding ice collisions alone would be sufficient to electrify a storm and produce lightning.

[4] Ziegler *et al.* [1991] and Ziegler and MacGorman [1994] used a three-dimensional version of the kinematic

¹Also at National Severe Storms Laboratory, Norman, Oklahoma, USA.

model of Ziegler [1985] [see also Ziegler *et al.*, 1986] to study electrification in a New Mexico thunderstorm and an Oklahoma tornadic supercell storm, respectively. Those studies used Doppler wind field analyses to drive the kinematics, but the microphysics and electrification were predicted. Both studies used a noninductive charge separation scheme based on Gardiner *et al.* [1985] and Jayaratne *et al.* [1983] that is also employed in the present study and described in greater detail later. In contrast, the studies of Scavuzzo and Caranti [1996] and Scavuzzo *et al.* [1998] injected arbitrary distributions of ice particles into a cloud consisting of small droplets only and with a steady wind field. While such studies can provide some insight into the behaviors of different laboratory-based results of noninductive charging (in this case, Takahashi [1978] and Saunders *et al.* [1991]), the lack of realistic microphysical development limits the conclusions that can be drawn.

[5] The two-dimensional storm electrification model (SEM) of Helsdon and Farley [1987] was used to simulate electrification in a Montana thunderstorm and for later studies [Randell *et al.*, 1994; Helsdon *et al.*, 2001]. The SEM also treats small ion processes and has parameterizations of the laboratory charging results of Takahashi [1978] (e.g., by Randell *et al.* [1994]) and Saunders *et al.* [1991]. Helsdon *et al.* [2001] (hereafter HWF) made the first comparison of laboratory-based parameterizations of charge separation in a full simulation model (i.e., with coupled dynamics and microphysics). They compared the initial electrification produced by three different noninductive charging schemes [Takahashi, 1978; Saunders *et al.*, 1991; Helsdon and Farley, 1987] and found significant differences between the results. Inductive (i.e., field dependent) charge separation was used in conjunction with the noninductive scheme of Helsdon and Farley [1987], but not with the other two noninductive schemes. The SEM was upgraded to three-dimensional for Helsdon *et al.* [2002], which demonstrated that small ion processes can be appreciable when noninductive charge separation is active but produce insignificant electrification on their own without an active noninductive charging process.

[6] One of the motivating factors for the present study was the need expressed by HWF for further comparison studies incorporating more recent laboratory work [e.g., Brooks *et al.*, 1997; Saunders and Peck, 1998] and in the context of a three-dimensional model. The work presented here explores further the comparison of charging parameterizations (older and newer) and includes intracloud (IC) and cloud-to-ground (CG) lightning to allow simulation beyond the initial electrification stage. A multicellular continental storm is simulated that is stronger and longer-lived than the case by HWF, but has similar initial precipitation formation. The sensitivity of storm charge structure to inductive charge separation between graupel and small cloud droplets is also investigated.

2. Laboratory Results of Noninductive Charging

[7] Beginning with the pioneering work of Reynolds *et al.* [1957], many laboratory studies of noninductive charging have focused on graupel undergoing riming growth and rebounding collisions with ice crystals [e.g., Takahashi, 1978; Takahashi and Miyawaki, 2002; Jayaratne *et al.*,

1983; Saunders *et al.*, 1991; Saunders and Peck, 1998]. Riming, the collection and rapid freezing of supercooled liquid droplets, has an unclear role in charge separation, but multiple laboratory studies have found that charge separation by rebounding graupel-crystal collisions is substantially reduced when the graupel is not experiencing riming growth. Simply the presence of supercooled droplets may be sufficient, however, as Jayaratne and Saunders [1985] found that charge separation could still be appreciable when the droplets were too small to be captured by the target. The relative growth rate hypothesis [Baker *et al.*, 1987; Baker and Dash, 1994] holds that the particle that is growing faster by vapor diffusion will gain positive charge from rebounding collisions. According to the hypothesis, then, neither particle necessarily has to be riming, but liquid droplets must be present to provide vapor for deposition growth. The graupel surface is affected by riming through latent heat release from freezing droplets and, if the droplets are evaporating, through the vapor release from the droplets before they freeze completely.

[8] The sign of charge acquired by simulated graupel has been found to be dependent on air temperature and cloud water content (CWC) or the rime accretion rate (*RAR*), as well as on other factors such as graupel surface temperature, the droplet size spectrum, and water droplet contaminants. Laboratory studies indicate that a temperature may exist, called the reversal temperature, at which the charge gained by graupel changes sign, all other factors being held constant. The results of different studies, however, are in conflict over the details of the charging dependence on temperature and CWC (or *RAR*), and under some circumstances a reversal temperature may not exist. Takahashi [1978] studied collisional charging with a chamber containing ice crystals and supercooled droplets. Rotating rods inside the chamber acted like graupel particles by collecting droplets (i.e., riming) and colliding with crystals. He found that the rimed rods gained positive charge from rebounding collisions with ice crystals at temperatures above -10°C regardless of CWC (Figure 1). At temperatures below -10°C , the rime gained positive charge at high and low CWC, but acquired negative charge at intermediate values. At a CWC of 1 g m^{-3} , the reversal in the polarity of acquired charge occurred at about -10°C .

[9] Jayaratne *et al.* [1983] obtained results that differed from Takahashi [1978]. They observed only negative charging of a riming particle at low CWC and low temperature. Charging of the graupel at temperatures greater than -10°C was negative for sufficiently low CWC. Furthermore, the reversal temperature at a CWC of 1.0 g m^{-3} was -20°C , or 10°C lower than found by Takahashi [1978].

[10] The results of Saunders *et al.* [1991] at the University of Manchester (UMIST) (in the same laboratory used by Jayaratne *et al.* [1983]) were also at variance with Takahashi [1978], though they reported positive charging at low temperature and CWC. Saunders *et al.* [1991] created a parameterization of their results for use in numerical model studies. The charging scheme determined the sign of charging based on the temperature and the effective CWC (*EW*), which is the CWC multiplied by the collection efficiency of the riming particle. The magnitude of charging also depended on *EW* and temperature and had a power-law dependence on both ice-crystal diameter and terminal fall

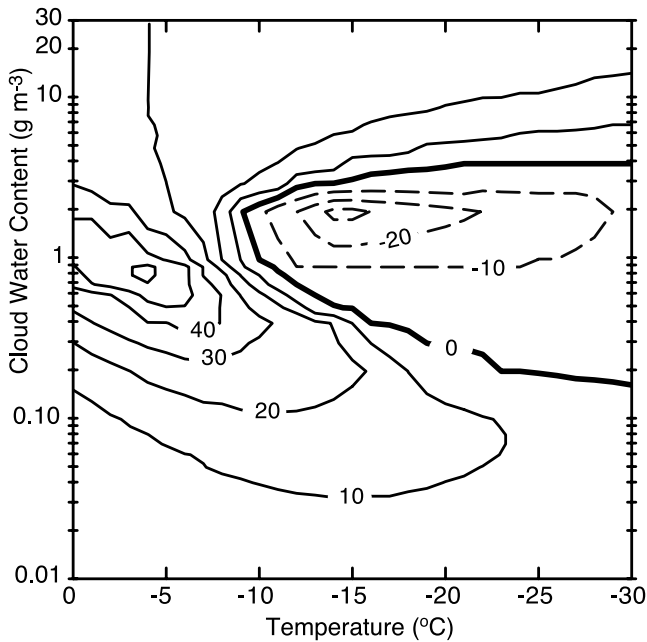


Figure 1. Takahashi (TAK) charging diagram [Takahashi, 1978], contoured from the lookup table [Helsdon et al., 2001], with charge separation in units of fC.

speed difference. Brooks et al. [1997] transformed the Saunders et al. [1991] parameterization to use the rime accretion rate, $RAR = EW \times V$ (where V is the graupel terminal speed). They omitted the positive charging region at low temperature and low EW for two reasons. First, they found their simple numerical cloud model was insensitive to that charging regime. Second, they cited the difficulty in performing charging tests reliably at very low values of RAR . Further exploration of the charging dependence on RAR was reported by Saunders and Peck [1998].

[11] Williams et al. [1991] attempted to relate charging to the graupel growth state (e.g., wet or dry growth). They found that the growth state regimes tended to match up with the different charging regimes found by Takahashi [1978], which included charging during wet growth. The equations they used to calculate the growth regimes were appropriate for the higher density rime they expected in the Takahashi [1978] experiment. They suggested that the Jayaratne et al. [1983] results were different because of the lower density rime expected from the lower riming rod speeds. Brooks and Saunders [1995] suggested that the continuous nucleation technique used by Takahashi [1978] may have contributed to a considerable overestimate of the cloud water content and thus wet growth likely was never actually achieved. Furthermore, Saunders and Brooks [1992] and Pereyra et al. [2000] have confirmed that charge separation becomes negligible during wet growth. Jayaratne [1993] noted that the equations for growth state used by Williams et al. [1991] would not be applicable to the laboratory-grown rime structures which are quite different in shape from natural graupel. When using appropriately modified equations, the hypothesis that the sign of charging depends on the growth state of the graupel appears not to be supported. Williams and Zhang [1996] looked more closely at the expected rime density in the Takahashi [1978] and

Saunders et al. [1991] experiments and again suggested that the differences in rime density might preclude direct comparison of the charging results. On the other hand, Jayaratne [1998] found that charging was not controlled by rime density.

[12] Some insight into the consistent differences between the results of Takahashi and the UMIST group was provided by Pereyra et al. [2000]. They asserted that the defining difference between the two sets of results comes from a difference in experimental method: Takahashi [1978] (and later Takahashi and Miyawaki [2002]) mixed separate clouds of droplets and ice crystals before hitting the target (mixed cloud method), whereas in the UMIST experiments ice crystals were grown in the droplet cloud (single cloud method). Pereyra et al. [2000] performed charge separation experiments using each method and achieved broad agreement with the previous results. They concluded that the mixed cloud method could create larger ice supersaturations and greater ice crystal growth rate, thereby affecting the conditions of charge separation. The fundamental factors that have led to different results are still unclear, however, and one of the open questions is which method, if either, best represents the conditions in a real cloud, or if certain clouds are better modeled by one method or the other. The difficulties of comparing different laboratory methods are further compounded by evidence that the droplet size spectrum may also play an important role in shifting the dependencies on temperature and cloud water content [e.g., Avila et al., 1998; Avila and Pereyra, 2000].

3. Thunderstorm Simulation Model

3.1. Numerics, Dynamics, and Microphysics

[13] The numerical simulation model used in the present study is the Straka Atmospheric Model (SAM) [Straka, 1989; Straka and Anderson, 1993a; Straka and Mansell, 2005; Mansell et al., 2002]. It is non-hydrostatic and fully compressible and based on the set of equations described by Klemp and Wilhelmson [1978]. Prognostic equations are included for momentum, pressure, potential temperature, and turbulent kinetic energy (as documented by Carpenter et al. [1998]). There are also conservation equations for (1) mixing ratios of water vapor and hydrometeors, (2) charge densities and ion concentrations, and (3) the age of cloud parcels and riming histories. The advection and diffusion numerics in the model all include a conservation principle. For momentum advection, the model uses a time-centered, quadratic (i.e., energy) conserving differencing scheme for the vertical, and a sixth-order local spectral scheme in the horizontal [Straka and Anderson, 1993b]. Scalar advection is performed with a forward in time, sixth-order, flux divergence-corrected, Crowley scheme [Tremback et al., 1987] with a monotonic filter [Leonard, 1991]. The diffusion parameterization is based on Deardorff [1980] and Moeng [1984] [see Carpenter et al., 1998]. Sedimentation uses the mass-weighted mean fall velocity with a sixth-order Crowley conservative flux scheme. The first-order “box-Lagrangian” sedimentation scheme of Kato [1995] is also available as an option but was not used in the present study.

[14] The microphysics package is a multi-category, single-moment bulk scheme [Straka and Mansell, 2005]. It

has two liquid hydrometeor categories (cloud droplets and rain) and ten ice categories characterized by habit and size: two ice crystal habits (column and plate), rimed cloud ice, snow (ice crystal aggregates), three graupel densities, frozen drops, small hail, and large hail. The three graupel particle densities are 300, 500, and 700 kg m⁻³ for low, medium, and high density graupel, respectively. Riming history is predicted for conversions among the various graupel density categories as well as the frozen drops category. The multiple precipitation ice categories allow a range of particle densities and fall velocities for simulation of a variety of convective storms with minimal parameter tuning. For example, at an air density of 1.0 kg m⁻³, the low, medium, and high density graupel categories have mass-weighted mean terminal velocities of 3.5 to 5 m s⁻¹, 4.5 to 7.5 m s⁻¹, and 5.5 to 9 m s⁻¹, respectively, for mixing ratios of 0.1 to 8 g kg⁻¹ [Straka and Mansell, 2005].

[15] Cloud droplets and cloud ice crystals (columns and plates) are treated as monodisperse distributions, and precipitation particles are assumed to have inverse exponential (IE) size distributions of diameter:

$$n_x(D) = n_{ox}e^{-D/\mathcal{D}_x} \quad (1)$$

where $n_x(D)$ (m⁻⁴) is the number concentration of particles (m⁻⁴) with diameter D of hydrometeor category x , and n_{ox} is the fixed intercept value. Note that \mathcal{D}_x here is the characteristic diameter [e.g., Cotton *et al.*, 1986], which is the inverse slope of the IE distribution, λ , so that $\mathcal{D}_x = \lambda^{-1}$.

3.2. Charge Conservation

[16] Each hydrometeor species n has an associated volume charge density Q_n that is predicted by integration of the charge continuity equation. Charge may also be transferred from one category to another as mass is transferred. For example, when a fraction of graupel mass melts to rain, the same fraction of the graupel charge is transferred to the rain category. Although local charge continuity is imposed, charge is not conserved globally when charge enters or leaves the domain by ion currents, CG lightning flashes, charged precipitation fallout, or by advection out through a lateral boundary. Small ion processes such as attachment and point discharge are included in the model in a manner similar to that of Chiu [1978] and Helsdon *et al.* [2002], as described in Appendix A.

[17] The continuity equation for charged hydrometeors is

$$\frac{\partial Q_n}{\partial t} = -\nabla \cdot (Q_n \mathbf{V}) + \nabla \cdot (K_h \nabla Q_n) + \frac{\partial (V_{t,n} Q_n)}{\partial z} + S_n \quad (2)$$

where K_h is the sub-grid eddy mixing coefficient for heat, assumed to be the same for the other scalars. The Prandtl number is set at 0.4 for all scalar variables. On the right-hand side of (2), the first term represents transport by advection (or current density divergence), the second term is for diffusion, the third term accounts for falling particle motion relative to the air motion and S_n is the sum of source and sink terms (e.g., charge separation and ion attachment). Advection, turbulent mixing, and sedimentation are calculated by the same methods as for the mass variables, including the use of mass-weighted mean fall velocity for sedimentation. Electrical forces are assumed to be insignif-

icant to the basic evolution of the storm and are not included.

[18] The net volume charge density Q_t at a grid point is the sum of all the individual charge categories (small ions and charged hydrometeors),

$$Q_t = e(n_+ - n_-) + \sum_n Q_n \quad (3)$$

where e is the small ion charge magnitude (electron charge), and n_+ and n_- are the positive and negative small ion number concentrations. The net charge is then the source term for the Poisson equation,

$$\nabla^2 \phi = -\frac{Q_t}{\epsilon} \quad (4)$$

where ϕ is the electric potential, and ϵ is the electrical permittivity of air (8.8592×10^{-12} F m⁻¹). The presence of hydrometeors in a particular grid volume involves such a small fraction of the air volume that the maximum increase in permittivity is estimated to be less than 1% and is therefore ignored.

[19] The vector electric field \mathbf{E} is found as the negative gradient of the potential:

$$\mathbf{E} = -\nabla \phi \quad (5)$$

[20] At the ground a Dirichlet boundary condition of $\phi = 0$ is used. The lateral boundaries have a Neumann condition of $E_n = \partial\phi/\partial n = 0$. The condition at the top is $\partial\phi/\partial n = E_{z,\text{FW}}$, where $E_{z,\text{FW}}$ is the fair weather electric field (equation (A2) in Appendix A). The artificial top and lateral boundaries act as “mirror” planes in which charge of the same sign is reflected. The effects of the mirror charges are diminished as the boundaries are moved farther away from the thunderstorm charges, so a larger domain is desirable for increased accuracy of the solution. On the other hand, one also wants the smallest domain needed for the dynamics and microphysics to minimize computational expense. The compromise implemented here is to use a smaller “dynamics domain” for all variables and use an extended “potential domain” for solving the Poisson equation. The potential domain is centered on the dynamics domain and is extended laterally and upward. The charge density in the extended zones is assumed to be the fair weather ion charge density. This arrangement allows for nonzero normal components of electric field at the boundaries of the “dynamics domain,” so that ion currents are possible through all boundaries. The Poisson equation is solved using the multigrid package MUDPACK [Adams, 1989].

3.3. Noninductive Charge Separation

[21] A fundamental requirement for using numerical cloud models is to include parameterizations of mechanisms by which hydrometeors acquire net charge. These mechanisms have been the subjects of a number of laboratory experiments. A hydrometeor might acquire a net charge from rebounding collisions with other particles or by capturing charged particles (ions or smaller hydrometeors). The two main classes of collisional charging mechanisms are inductive and noninductive. Inductive, or polarization,

charging requires a pre-existing electric field to induce charge on the surfaces of the colliding particles. Noninductive mechanisms operate without regard to an external electric field.

[22] The model includes five parameterizations of noninductive charge separation via rebounding graupel-ice collisions. The ‘‘TAK’’ parameterization uses the results from *Takahashi* [1978] with the addition of a factor to vary the charge separation per rebounding collision based on impact speed and crystal size [*Takahashi*, 1984]. The Gardiner/Ziegler (GZ) scheme is adapted from *Ziegler et al.* [1991] and is based on *Gardiner et al.* [1985] and *Jayaratne et al.* [1983]. The third scheme (S91) is from *Saunders et al.* [1991] with modifications of HWF. The last two parameterizations utilize the idea of the critical rime accretion rate RAR_{crit} that divides positive and negative charging conditions. The first is the Riming Rate (RR) parameterization, which is based on *Brooks et al.* [1997] with modifications to the critical rime accretion rate RAR curve following *Saunders and Peck* [1998] and the charging results for smaller cloud droplets in *Saunders et al.* [1999]. The second RAR -based scheme is from *Saunders and Peck* [1998] (hereafter SP98). Details of each scheme are given in the following subsections.

[23] The model microphysics has six large ice hydrometeor categories (three graupel categories, two hail sizes, and frozen drops), which for simplicity will be referred to collectively as graupel in the context of charge separation. Charge separation rates are calculated for rebounding collisions of graupel with cloud ice and aggregates. Interactions between the graupel categories may be important for charge separation but are not yet considered because of the lack of laboratory studies on graupel-graupel collisional charging. Laboratory results to date are directly applicable only to interactions between riming precipitation ice particles (i.e., graupel) and unrimed, vapor-grown ice crystals. Although small rimed ice crystals are included in the charging equations in the model, it is assumed that the rime accretion rates of the cloud ice are much less than the graupel rime accretion rates so that the laboratory results are still approximately valid. No charge separation is calculated for rebounding collisions between snow aggregates and ice crystals in the present study, although the option exists and may be important in the stratiform region of mesoscale convective systems.

[24] The general formulation for the noninductive charge separation rate $\partial Q_{xy}/\partial t$ between ice hydrometeor classes x and y is

$$\frac{\partial Q_{xy}}{\partial t} = \int_0^\infty \int_0^\infty \frac{\pi}{4} \delta q'_{xy} (1 - E_{xy}) |V_x - V_y| \times (D_x + D_y)^2 n_x(D_x) n_y(D_y) dD_x dD_y \quad (6)$$

where D_x and D_y are the diameters of the colliding particles, E_{xy} is collection efficiency, $|V_x - V_y|$ is the relative fall speed, n_x and n_y are number concentrations, and $\delta q'_{xy}$ is the charge separated per rebounding collision. In general, $\delta q'_{xy}$ may be a function of ice-crystal diameter, impact speed, cloud water content, and temperature. The collection efficiency E_{xy} is the product of the collision efficiency (ϵ_{coll} , assumed to be unity) and the probability of sticking given a collision (ϵ_{stk}). In wet-growth mode, $E_{g,y} = 1$ and no charge separation occurs. For interactions between snow or

ice crystals and graupel in dry-growth mode, $E_{g,y} = 0.01 \exp(0.1 T_C)$, where T_C is the temperature in $^\circ\text{C}$. At small crystal diameters, the collision efficiency can become much smaller than unity [e.g., *Keith and Saunders*, 1989], but this effect is not yet incorporated into the model. Another potential source of error is the assumed very low sticking probability, which results in a high ‘‘event probability’’ (EP; the product $\epsilon_{coll}\epsilon_{sep}$, where $\epsilon_{sep} = 1 - \epsilon_{stk}$ is the separation probability), whereas *Jayaratne et al.* [1983] and *Keith and Saunders* [1989] determined EP values on the order of 0.2. An improved treatment of the EP is planned for the future.

[25] As it stands, equation (6) is not a tractable integrand. The equation can be approximated and simplified by assuming a form for $\delta q'_{xy}$ that can be pulled out of the integral. Also, the fall speed difference is approximated by the difference of mass-weighted mean fall speeds. The collection efficiency is assumed to be constant. Multiplying and dividing by E_{xy} then isolates the number concentration collection rate integral (n_{xacy}):

$$\frac{\partial Q_{xy}}{\partial t} = \beta \delta q_{xy} (1 - E_{xy}) E_{xy}^{-1} (n_{xacy}) \quad (7)$$

where,

$$n_{xacy} = E_{xy} |\bar{V}_y - \bar{V}_x| \times \int_0^\infty \int_0^\infty \frac{\pi}{4} (D_x + D_y)^2 n_x n_y dD_x dD_y \quad (8)$$

where δq_{xy} is now a representative (weighted average) separated charge per rebounding collision and $(1 - E_{xy})$ represents the rebound probability. Each of the noninductive charging schemes uses the monodisperse diameter D for pristine ice crystals (plates and solid columns) but the characteristic diameter \mathcal{D}_n to represent the average size of an inverse exponential (IE) distribution (e.g., rimed cloud ice and ice aggregates). The number concentration collection rate n_{xacy} is calculated by an analytical approximation. For an inverse exponential distribution category (x_e) interacting with a monodisperse distribution (y_m , e.g., ice crystals) the number concentration collection rate is

$$n_{x_e a c y_m} = \frac{\pi}{4} E_{xy} n_y n_x |\bar{V}_x - V_{m,y}| \times \left[\Gamma(3) \mathcal{D}_{n,x}^2 + 2\Gamma(2) \mathcal{D}_{n,x} D_y + \Gamma(1) D_y^2 \right] \quad (9)$$

Similarly, for an IE distribution (x_e) interacting with another IE distribution (y_e , e.g., rimed ice or snow) the number concentration collection rate is

$$n_{x_e a c y_e} = \frac{\pi}{4} E_{xy} n_y n_x |\bar{V}_x - \bar{V}_y| \left[\Gamma(3) \Gamma(1) \mathcal{D}_{n,x}^2 + 2\Gamma(2) \Gamma(2) \mathcal{D}_{n,x} \mathcal{D}_{n,y} + \Gamma(1) \Gamma(3) \mathcal{D}_{n,y}^2 \right] \quad (10)$$

[26] Few quantitative results are available on charge separation at temperatures less than -30°C . (One example is *Saunders and Peck* [1998], which examined the sign of charging, but not quantity, at lower temperature.) Therefore, lacking experimental guidance, charging at low temperature has been limited by an arbitrary factor β , where

$$\beta = \begin{cases} 1 & : T > -30^\circ\text{C} \\ 1 - [(T + 30)/13]^2 & : -43^\circ\text{C} < T < -30^\circ\text{C} \\ 0 & : T < -43^\circ\text{C} \end{cases} \quad (11)$$

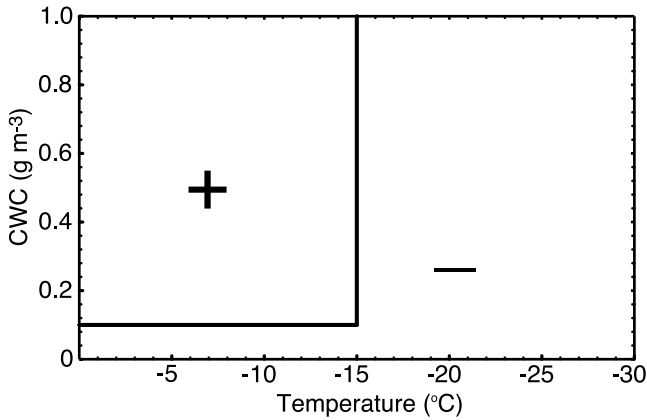


Figure 2. Charging zones of the GZ [Gardiner *et al.*, 1985; Ziegler *et al.*, 1991; Jayaratne *et al.*, 1983] noninductive ice-ice parameterization. Here, the reversal temperature (for $CWC > 0.1 \text{ g m}^{-3}$) is set at $T_r = -15^\circ\text{C}$.

The low-temperature cut-off is made at -43°C because in the model all cloud droplets are homogeneously frozen so that no further riming occurs.

[27] To prevent unreasonably large charging and lightning flash rates, the maximum magnitude of δq is limited to 50 fC for rebounding graupel-snow collisions and 20 fC for graupel-crystal interactions, similar to Ziegler *et al.* [1991]. For comparison, in Ziegler *et al.* [1991], rebounding graupel-crystal collisions separated a fixed value of only ± 0.1 fC. These upper bounds on charge separation help keep the rates from different parameterizations to stay within the same order of magnitude and avoid the gross mismatch of charging rates found by HWF.

3.3.1. TAK Scheme

[28] The TAK noninductive charging parameterization uses the laboratory data directly from Takahashi [1978]. The charge per collision $\delta q'$ is calculated from a lookup table of Takahashi's data as implemented by Randell *et al.* [1994] and HWF. Although the approach here (as in HWF) treats the data as charge per rebounding collision, the assumed rebound efficiency is close enough to the collision efficiency that the difference is small. The table covers a temperature range of 0°C to -30°C and cloud water content from 0.01 to 30 g m^{-3} . For temperatures lower than -30°C , the charge separation values at -30°C were used. Charging dependence on crystal size and fall speed are parameterized by multiplying the value obtained from the table by a factor α , as in Takahashi [1984]:

$$\alpha = 5.0(D_1/D_0)^2 \bar{V}_g/V_0 \quad (12)$$

where D_1 is the diameter of the ice crystal or snow particle, \bar{V}_g is the mass-weighted mean terminal fall speed of graupel, and $D_0 = 100 \mu\text{m}$ and $V_0 = 8 \text{ m s}^{-1}$. This factor was based on the work of Marshall *et al.* [1978], but the scheme could be updated to incorporate the more recent results of Keith and Saunders [1990] regarding dependence on crystal size and impact speed. As in Takahashi [1984], the value of α is not allowed to be greater than 10.0 (i.e., $\alpha \leq 10.0$). Thus, for the TAK scheme we have

$$\delta q = \alpha \delta q' \quad (13)$$

where $\delta q'$ is the value interpolated from the lookup table.

3.3.2. GZ Scheme

[29] The Gardiner/Ziegler (GZ) scheme is adapted from Ziegler *et al.* [1991] and is based on Gardiner *et al.* [1985], who extrapolated the laboratory results of Jayaratne *et al.* [1983] to obtain a charge separation equation for atmospheric conditions:

$$\delta q' = 7.3 D_1^4 \Delta V^3 \delta L f(\tau) \quad (14)$$

where D_1 is the ice crystal or snow particle diameter in meters and ΔV is the crystal impact speed (i.e., relative fall speed) in m s^{-1} . In the model, δq is approximated as

$$\delta q = 7.3 D_1^4 |\bar{V}_g - \bar{V}_1|^3 \delta L f(\tau) \quad (15)$$

where \bar{V}_g and \bar{V}_1 are the mass-weighted mean terminal speeds for graupel and cloud ice or snow, respectively, and D_1 again is the diameter for the particular cloud ice or snow category being considered. (The characteristic, or average, diameter D_n for an IE distribution is used for snow and rimed ice.) Here again, the size and impact speed dependency could be modified to use the Keith and Saunders [1990] results. The dependence on cloud water content (CWC, in g m^{-3}) is given by δL as follows:

$$\delta L = \begin{cases} CWC - CWC_{\text{crit}} & : T > T_r \\ CWC & : T < T_r \text{ and } q_c \geq 10^{-6} \text{ kg/kg} \\ 0 & : q_c < 10^{-6} \text{ kg/kg} \end{cases} \quad (16)$$

where $CWC_{\text{crit}} = 0.1 \text{ g m}^{-3}$, q_c is the cloud water mixing ratio (the ratio of the water substance mass to the mass of air in a parcel), and T_r is the reversal temperature (Figure 2). The function $f(\tau)$ was adapted from Gardiner *et al.* [1985] by Ziegler *et al.* [1991]:

$$f(\tau) = -1.7 \times 10^{-5} \tau^3 - 0.003 \tau^2 - 0.05 \tau + 0.13 \quad (17)$$

where $\tau = (-21/T_r)(T - 273.16)$ is the scaled temperature used by Ziegler *et al.* [1991] to allow the reversal temperature T_r to be varied. In their modeling study of a small New Mexico thunderstorm, Ziegler *et al.* [1991] found that using $T_r = -21^\circ\text{C}$ resulted in a charge distribution having negative above positive charge (a so-called “negative dipole”). Measurements in the storm, however, indicated positive charge over negative (a “positive dipole”) which is what is typically observed in many storms. Setting $T_r = -10^\circ\text{C}$ resulted in positive charge above negative in the simulated charge structure, suggesting that the main charging zone was in the -10 to -20°C layer. The supercell storm study of Ziegler and MacGorman [1994] used the same numerical model as Ziegler *et al.* [1991] and obtained a positive dipole charge structure with $T_r = -15^\circ\text{C}$, which is the value adopted for the present study.

3.3.3. S91 Scheme

[30] Saunders *et al.* [1991] (S91) published a noninductive charge separation parameterization that included the results of Keith and Saunders [1990] for dependence on crystal size and impact velocity. The implementation here follows HWF. One difference from the TAK scheme is that the Saunders *et al.* [1991] results were based on effective cloud water content EW rather than the total CWC. The EW

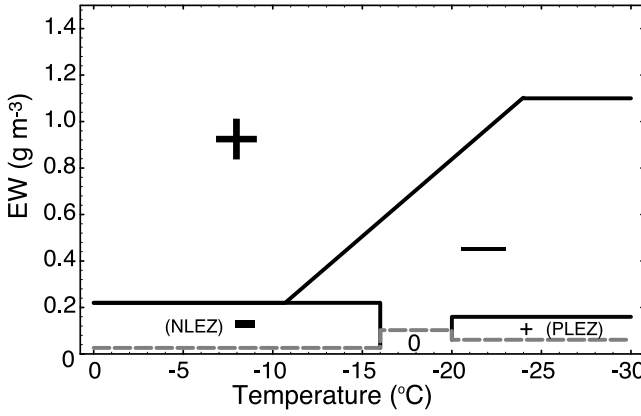


Figure 3. Plot of the charging zones of the S91 [Saunders *et al.*, 1991] noninductive ice-ice parameterization. The positive and negative low- EW zones are indicated by PLEZ and NLEZ, respectively. (No charge separation occurs for conditions below the dashed line.)

is calculated as the cloud water content multiplied by the droplet collection efficiency of the graupel, which in the model is determined from a fit of the experimental data of Mason [1971] (see Straka and Mansell [2005] for details) and has a range of values from about 0.6 to 1.0.

[31] The positive and negative charging zones at low effective water (EW) content are reduced as in HWF: The negative zone is reduced to 20% of the original value and the positive zone to 10%. (These zones are labeled NLEZ and PLEZ in Figure 3 for the negative and positive low- EW zones.) Unlike in HWF, however, no need was found to reduce the overall charging rate. Some tests were made with no reduction to the low- EW zones, and it was found that the limits on charge per rebounding collision (section 3.3) capped the charging rates to about the same levels as the HWF reductions. To test the overall importance of the PLEZ, an option was added (S91*) to replace it by normal negative charging of graupel, which is relatively weak for those conditions.

3.3.4. RAR -Based Schemes

[32] The last two noninductive parameterizations are based on Brooks *et al.* [1997], Saunders *et al.* [1999], and Saunders and Peck [1998]. Brooks *et al.* [1997] transformed the parameterization of Saunders *et al.* [1991] to be in terms of the rime accretion rate RAR instead of EW , where RAR is the EW multiplied by the graupel mean relative fall velocity. They constructed a curve of critical RAR (RAR_{crit}) at which the charging of graupel changes sign for a particular temperature (negative at lower RAR and positive for higher). Saunders and Peck [1998] conducted further experiments to determine RAR_{crit} at a larger range of temperatures. The two parameterizations based on these results differ only in the function used to define RAR_{crit} . The first will be referred to as the Riming Rate (RR) parameterization and the second as SP98.

[33] The RR and SP98 parameterizations both use charging equations adapted from Brooks *et al.* [1997]. The mean separated charge per rebounding collision is given by

$$\delta q = BD_{n,1}^a (\bar{V}_g - \bar{V}_1)^b q_{\pm}(RAR) \quad (18)$$

where \bar{V}_g and \bar{V}_1 are the mass-weighted mean terminal speeds for graupel and cloud ice (or snow), respectively, and B , a , and b are constants that depend on crystal size as shown in Table 1 (also used in the S91 scheme). The charge separation equations, $q(RAR, T)$ from Brooks *et al.* [1997] have been altered for the present study so that they smoothly approach zero at $RAR = RAR_{crit}$. For positive charging of graupel ($RAR > RAR_{crit}$),

$$q_+(RAR) = 6.74(RAR - RAR_{crit}) \quad (19)$$

For negative charging ($0.1 \text{ g m}^{-2} \text{ s}^{-1} < RAR < RAR_{crit}$),

$$q_-(RAR) = 3.9(RAR_{crit} - 0.1) \times \left(4 \left[\frac{RAR - (RAR_{crit} + 0.1)/2}{(RAR_{crit} - 0.1)} \right]^2 - 1 \right) \quad (20)$$

Note that there is an implicit temperature dependence since RAR_{crit} varies with temperature. The negative charging equation (20) shifts the parabolic function given in Brooks *et al.* [1997] to fit between the limits of $0.1 \text{ g m}^{-2} \text{ s}^{-1}$ and RAR_{crit} , removing the discontinuity at RAR_{crit} in the original formulation. Charging is set to zero for $RAR < 0.1 \text{ g m}^{-2} \text{ s}^{-1}$.

3.3.4.1. SP98 Scheme

[34] The SP98 scheme is an adaptation of the parameterization of Saunders and Peck [1998]. The critical RAR curve for the SP98 scheme ($SP98_{crit}$) delineates the positive and negative graupel charging zones as a function of RAR and temperature. It is shown in Figure 4 and given by a piece-wise continuous function:

$$SP98_{crit}(T) = \begin{cases} s(T) & : T > -23.7^\circ\text{C} \\ k(T) & : -23.7 > T > -40.0^\circ\text{C} \\ 0 & : T \leq -40.0^\circ\text{C} \end{cases} \quad (21)$$

where $s(T)$ is the sixth-order polynomial functional fit given by Saunders and Peck [1998],

$$s(T) = 1.0 + 7.9262 \times 10^{-2}T + 4.4847 \times 10^{-2}T^2 + 7.4754 \times 10^{-3}T^3 + 5.4686 \times 10^{-4}T^4 + 1.6737 \times 10^{-5}T^5 + 1.7613 \times 10^{-7}T^6 \quad (22)$$

The function $s(T)$ becomes negative for $T < -32.47^\circ\text{C}$, but liquid cloud droplets can exist at temperatures at least as low as -37.5°C [Rosenfeld and Woodley, 2000] and thus riming and presumably also charge separation can occur.

Table 1. Values of Constants for S91, Riming Rate (RR), and SP98 Charging Schemes^a

| Charge Sign | Crystal Size, μm | B | a | b |
|-------------|-----------------------------|----------------------|------|-----|
| + | <155 | 4.9×10^{13} | 3.76 | 2.5 |
| + | 155–452 | 4×10^6 | 1.9 | 2.5 |
| + | >452 | 52.8 | 0.44 | 2.5 |
| – | <253 | 5.24×10^8 | 2.54 | 2.8 |
| – | >253 | 24 | 0.5 | 2.8 |

^aFrom Brooks *et al.* [1997].

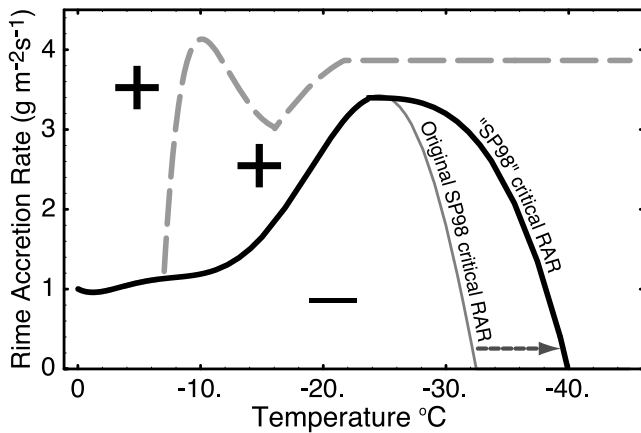


Figure 4. Plot of the critical rime accretion rate curve (solid black) used in the SP98 [Saunders and Peck, 1998] noninductive ice-ice parameterization. Graupel charges positively at rime accretion rates above the curve and negatively below. (The RR curve is shown as a dashed line and the curve of function $s(T < -23.7)$ is shown as a thin solid gray line.)

Therefore, the function $k(T)$ is used for $T < -23$ to keep the critical RAR positive down to $T < -40^\circ\text{C}$:

$$k(T) = 3.4 \left[1.0 - \left(\frac{|T + 23.7|}{-23.7 + 40.0} \right)^3 \right] \quad (23)$$

which is a cubic decrease from $k(-23.7) = s(-23.7)$ to $k(-40) = 0$. This scheme was also tested with the input value of RAR reduced by a factor of 0.5 (referred to as SP98r).

3.3.4.2. RR Scheme

[35] The Riming Rate (RR) scheme roughly follows the Brooks *et al.* [1997] recasting of the Saunders *et al.* [1991] parameterization, which converted EW to RAR and dropped the low- EW zones. The critical RAR curve for the RR scheme is shown in Figure 5 and given by the piece-wise continuous function

$$RR_{\text{crit}}(T) = \begin{cases} s(T) & : T > -7.0^\circ\text{C} \\ g(T) & : -7.0 > T > -16.0^\circ\text{C} \\ h(T) & : -16.0 > T > -21.7^\circ\text{C} \\ h(-21.7) & : T < -21.7^\circ\text{C} \end{cases} \quad (24)$$

where $s(T)$ is the same as above and

$$g(T) = s(T) + (8/3)|T + 7| \exp[(T + 7)/3] \quad (25)$$

$$h(T) = 4 \left(1.0 - [(T + 25)/18]^2 \right) \quad (26)$$

are approximate fits to the critical riming rate curve presented in Saunders *et al.* [1999] for smaller droplets. Following the suggestion of Brooks *et al.* [1997], at temperatures below the range of laboratory data (i.e., below about -30°C) the charging values at $T = -30^\circ\text{C}$ are used.

3.4. Inductive Charging

[36] Inductive, or polarization, charging results from rebounding particle collisions in the presence of an electric

field. The electric field polarizes the particles by forcing ions of opposite sign to accumulate at opposite sides, and charge may be transferred between particles when they collide and separate. We assume that inductive charging is ineffective for ice-ice collisions because the lower conductivity of ice and short contact times prevent electrical currents from transferring appreciable charge [Latham and Mason, 1962; Gaskell, 1981]. Enhanced coalescence by the electric field makes it unlikely that liquid particles will rebound in regions of even moderate field magnitudes [Jennings, 1975]. The only inductive interaction considered in the present model is rebounding collisions of graupel and cloud droplets, and then only if the graupel is in a dry growth mode. In a wet growth mode, it is assumed that droplets would coalesce with the surface liquid layer and not have a chance to rebound. It is conceivable to calculate inductive charge separation for liquid drops being shed from hailstones, but this is not currently treated in the model. Aufdermaur and Johnson [1972] found a rebound rate of only 1 to 10 per 1000 collisions between droplets and an ice pellet, and the droplets that did rebound generally lost some mass. The loss of mass suggested partial freezing of the droplet to the ice and thus that growth was in a dry mode. Sartor [1981], on the other hand, pointed out that the ice pellet grown by Aufdermaur and Johnson [1972] had many crevices which could capture droplets and did not resemble naturally-occurring graupel. Sartor [1981] showed photographic evidence that a higher rebound rate might be achieved and that droplets could rebound from non-grazing trajectories when the graupel pellet had a round shape with a rough surface, but did not provide quantitative data.

[37] It is generally agreed that inductive charging alone would be insufficient to strongly electrify a storm because the mechanism is far too weak at fair-weather electric field magnitudes. Noninductive charge separation, on the other hand, does appear to be capable by itself of electrifying a storm to the point of lightning. Brooks and Saunders [1994]

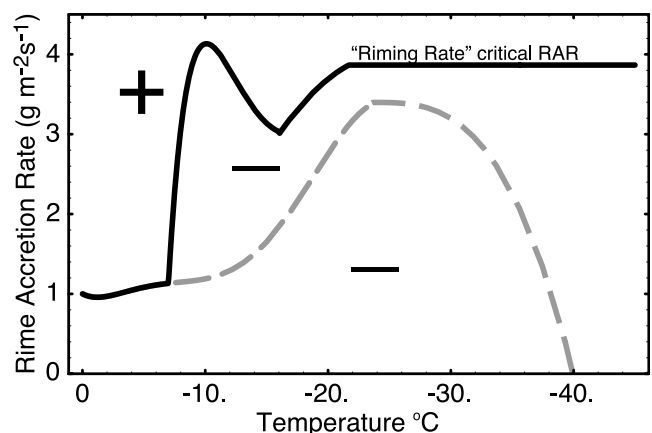


Figure 5. Plot of the critical rime accretion rate curve (solid black) used in the Riming Rate (RR) noninductive ice-ice parameterization [Brooks *et al.*, 1997; Saunders *et al.*, 1999; Saunders and Peck, 1998]. Graupel charges positively at rime accretion rates above the curve and negatively below. (The SP98 curve is shown as a dashed line for comparison.)

tested the inductive mechanism by dropping tiny metal spheres through a droplet cloud in an electric field. They found an average charge separation that was about half the theoretical calculations of *Mason* [1988], suggesting that the mechanism could be effective in thunderstorms with strong electric fields. So the question remains open as to what role inductive charging might have in thunderstorm electrification, and for this reason we have included the mechanism in the model.

[38] The inductive charging formulation used in the present study is equivalent to that of *Ziegler et al.* [1991] but is rewritten here in terms of characteristic diameter and mass-weighted mean fall speed:

$$\frac{\partial Q_g}{\partial t} = (\pi^3/8) \left(\frac{6.0 \bar{V}_g}{\Gamma(4.5)} \right) E_{gc} E_r n_{t,c} n_{0g} D_c^2 \times \left[\pi \Gamma(3.5) \epsilon \langle \cos \theta \rangle E_z \mathcal{D}_{n,g}^2 - \Gamma(1.5) Q_g / (3 n_{t,g}) \right] \quad (27)$$

where D_c is the cloud droplet diameter, E_{gc} is the collision efficiency, E_r is the rebound probability, $n_{t,c}$ and $n_{t,g}$ are the total cloud water and graupel number densities, \bar{V}_g is the mass-weighted mean fall speed of graupel, $\Gamma(x)$ is the complete gamma function, $\mathcal{D}_{n,g}$ is the characteristic diameter of graupel, n_{0g} is the number concentration intercept for graupel, $\langle \cos \theta \rangle$ is the average cosine of the angle of rebounding collision, E_z is the vertical component of the electric field, and ϵ is the permittivity of air. The second term in the square brackets represents the effect of the pre-existing charge carried by graupel Q_g on the induced charge on the droplet. Since droplets greatly outnumber graupel, it is assumed that the rebounding droplets are initially neutral and experience only one rebounding collision with graupel. *Ziegler et al.* [1991] used an effective $E_r = 0.0022$ and $\langle \cos \theta \rangle = 0.1$. These values were consistent with an event probability at the low end of the range given by *Aufdermaur and Johnson* [1972] (i.e., around 1:1000) and resulted weak inductive charging. Higher values were tested in the present study to examine the possible importance of inductive charging for parameters closer to the high end of *Aufdermaur and Johnson* [1972] (i.e., event probability on the order of 1:100). For “moderate” inductive charging $E_r = 0.007$ and $\langle \cos \theta \rangle = 0.2$, while for “strong” charging $E_r = 0.015$ and $\langle \cos \theta \rangle = 0.45$. The assumed rebound probabilities E_r are within the range of experimental results, which vary from as low as 0.1% to 1.0% [*Aufdermaur and Johnson*, 1972] for bouncing collisions to as large as about 10% [*Gaskell*, 1981] for grazing trajectories.

[39] Model tests were performed with no precipitation charging at all (charging by ion attachment only), and with inductive charging in conjunction with ion processes. The ions-only test resulted in maximum electric field magnitudes on the order of 200 V m^{-1} (fair-weather magnitudes), consistent with the model results of *Helsdon et al.* [2002], who tested the convective charging theory [*Grenet*, 1947; *Vonnegut*, 1953], also known as the Grenet-Vonnegut mechanism [*MacGorman and Rust*, 1998]. (An English reprint of *Grenet* [1947] is available as *Grenet* [1993].) For the second test, “strong” inductive charging (graupel-droplet only) was added, resulting again in maximum field magnitudes of about 200 V m^{-1} . These results support the

current consensus that inductive charge separation acting alone cannot cause significant thunderstorm electrification.

3.5. Lightning Parameterization

[40] A parameterization of lightning discharges must be used to limit the electric field to reasonable magnitudes and allow a complete storm life cycle to be simulated. The present study uses the branched lightning discharge scheme of *Mansell et al.* [2002], which is capable of producing IC flashes and both polarities of CG flashes, depending on the thunderstorm charge structure. As in *MacGorman et al.* [2001], a flash is initiated when the electric field exceeds a height-dependent threshold E_{init} that decreases exponentially with increasing altitude: $E_{\text{init}} = 201.7 \exp(-z/8.4)$, where z is the altitude in km [*Marshall et al.*, 1995]. *Mansell et al.* [2002] found that the lightning scheme seemed to produce too few CG flashes, so two adjustments were made: (1) Since the channel propagation threshold is a given fraction of E_{init} , the magnitude of E_{init} is limited to 125 kV m^{-1} so that propagation is not unduly suppressed at lower altitudes. (2) An altitude threshold was used to determine whether to declare a flash to be a CG without requiring that the channel propagate all the way to ground on its own. In the present study the height threshold is 2200 m, but a further criterion has been added to check that the electrical potential of the branch has the same sign as the charge carried by the branch, otherwise the discharge is not automatically brought to ground. The electric potential changes along the channel because of the simulated electrical resistance represented by the internal electric field. Thus it is possible, for example, that a negative leader tip can eventually acquire a positive potential but would nevertheless be lower than the ambient potential, and such a channel would not be connected to ground if it propagated down to the specified height threshold. The polarity of a CG flash is determined by the polarity of the branch that reaches the ground.

4. Storm Initiation and Evolution

[41] An analytical thermodynamic sounding was used following *Weisman and Klemp* [1982], with a boundary layer vapor mixing ratio of 13.5 g kg^{-1} , resulting in convective available potential energy of about 1630 J kg^{-1} . The environment had a half-circle hodograph ($U_s = 20 \text{ m s}^{-1}$) with the wind shear confined to the lowest 5 km, as in *Weisman and Klemp* [1984]. The computational domain was 45 km by 45 km by 17.5 km, with constant horizontal grid spacing of 500 m and vertical spacing of 200 m at the surface stretching to a constant 500 m above 8.75 km. The concentration of cloud condensation nuclei (CCN) was set at 10^9 m^{-3} , and the droplet dispersion was set at $\phi = 0.15$, consistent with a continental storm [e.g., *Hobbs and Rangno*, 1985]. Convection was initiated by a warm spheroid with a central temperature perturbation of 0.9 K. The spheroid radii were $5 \times 5 \times 1.5 \text{ km}$. Random perturbations were added to the warm bubble to increase entrainment and mixing in the initial thermal. Some microphysical development of this multicell storm simulation is also described in *Straka and Mansell* [2005].

[42] The modeled storm was multicellular and had a lifetime of about 2 hr. It was chosen as a middle-of-the-

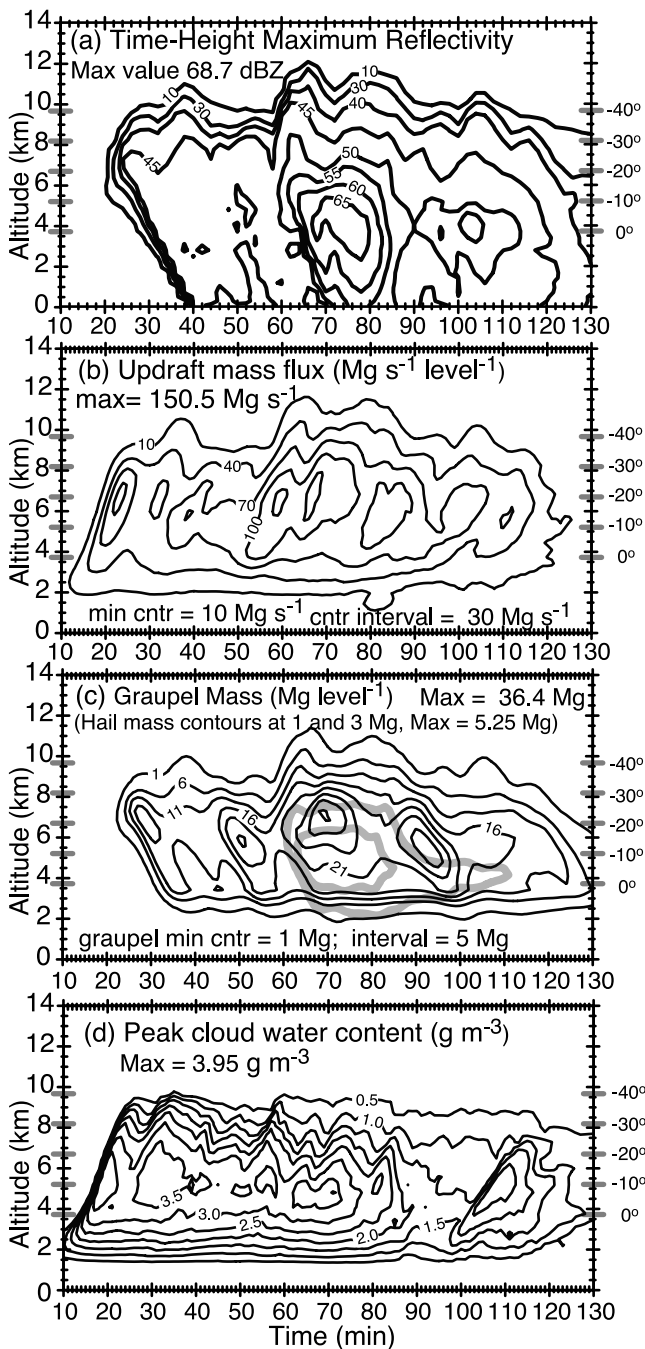


Figure 6. Time-height plots showing the multicell storm evolution. (a) Maximum reflectivity (10, 30 dBZ, and increments of 5 from 40 to 65 dBZ). (b) Horizontally integrated updraft mass flux (Mg s^{-1} per model level, where 1 Mg = 1000 kg). (c) Total graupel (black) and total hail (gray) masses (Mg) per model level. (d) Peak cloud water content (g m^{-3}) per model level.

road case between short-lived, highly variable single-cell storms and long-lived supercell storms. The simulation had many of the characteristics typical of Colorado storms [Dye *et al.*, 1974], which are characterized by precipitation-free updraft base and cloud droplets that are too small for effective growth by collision-coalescence. (The cloud base, however, is more typical of central/southern plains storms,

i.e., it is lower than for usual Colorado storms.) The high prescribed CCN concentration guaranteed small rain droplet diameters and effectively turned off the warm rain process (i.e., rain autoconversion) in the model [Dye *et al.*, 1974]. A similar approach was taken by HWF to shut down the warm rain process (J. Helsdon, personal communication, 2005) in a high-plains continental storm. Therefore the ice process was the dominant mode of precipitation formation.

[43] The dynamical and microphysical evolution of the multicell storm is summarized in Figure 6. The updraft mass flux reveals a series of updraft pulses (20, 30, 37, 52, and 65 min). The first four pulses were connected to a relatively steady updraft base at 3 to 4 km AGL, following the “weak evolution” model of Foote and Frank [1983] based on the Westplains, Colorado, storm, observed during the National Hail Research Experiment in 1976. (In the “strong evolution” model each updraft has a new base.) Accompanying each updraft cell was an increase in graupel mass, which shifted toward lower levels as a cell decayed.

[44] The precipitation from the first three updraft cells tended to fall far enough outside the updraft to avoid being drawn back into the updraft (i.e., precipitation recycling did not yet occur). The stronger successive cells, occurring around 52 to 75 min, however, did reingest graupel and meltwater rain at lower levels into their updrafts, producing higher integrated graupel mass, hail, and higher reflectivity around 60–85 min [Straka and Mansell, 2005]. The peak updraft values for the cells were in the range of 27 to 35 m s^{-1} . Three successively weaker updrafts are apparent in Figure 6b at 80, 100, and 110 min. The pattern of individual cells having increasing echo tops, then peaking, then following cells with decreasing tops (Figure 6a) is similar, for example, to the storm observations of Brown and Meitin [1994] during the North Dakota Thunderstorm Project.

5. Sensitivity Tests

[45] The sensitivity study of Helsdon *et al.* [2001] (HWF) was an important step in the use of models to test the results of graupel-ice crystal charge separation in the laboratory. The present model greatly expands upon HWF with a three-dimensional model (instead of two-dimensional), inclusion of lightning, and greater number of combinations of charge separation parameterizations. As stated earlier, one reason to simulate lightning discharges is to restrict the electric field magnitudes to within observed values, allowing simulations to continue past the point of initial strong electrification and through a full storm life-cycle. The lightning is also important because it naturally picks out the significant charge regions that might be inferred, for example from lightning mapping observations [e.g., Rison *et al.*, 1999]. Recognizing the importance of ice crystal size and concentration, HWF also examined the effect of changing some assumed parameters controlling ice crystal concentration in their model. The present study also looks at some effects of the treatment of ice crystal concentration.

[46] Three general sensitivities to the charge separation parameterizations are tested. The first examines differences resulting from the five noninductive charge separation schemes. The second varies the efficiency of inductive charge separation through the rebound efficiency E_r and average of the cosine of the rebound angle $\langle \cos \theta \rangle$. Three

Table 2. Summary of Total Lightning Flashes for Each Simulation^a

| Charging Scheme | Number of Flashes | | | Coulombs Discharged | | |
|-----------------|-------------------|-----|-----|---------------------|-----|------|
| | IC | +CG | -CG | IC | +CG | -CG |
| TAK/off/10 | 181 | 0 | 0 | 1,470 | 0 | 0 |
| TAK/mod/10 | 154 | 0 | 4 | 1,300 | 0 | -51 |
| TAK/str/10 | 358 | 0 | 27 | 2,250 | 0 | -133 |
| TAK/off/50 | 700 | 0 | 16 | 4,510 | 0 | -85 |
| TAK/off/200 | 3253 | 0 | 37 | 20,240 | 0 | -231 |
| GZ/off/10 | 416 | 1 | 0 | 2,800 | 7 | 0 |
| GZ/mod/10 | 338 | 1 | 1 | 2,400 | 5.7 | -8 |
| GZ/str/10 | 513 | 0 | 14 | 3,130 | 0 | -54 |
| GZ/off/50 | 1545 | 3 | 10 | 8,570 | 10 | -38 |
| S91/off/10 | 139 | 2 | 0 | 990 | 6 | 0 |
| S91/mod/10 | 124 | 0 | 0 | 820 | 0 | 0 |
| S91/str/10 | 256 | 2 | 5 | 1,360 | 3 | -20 |
| S91/off/50 | 633 | 6 | 6 | 3,210 | 14 | -22 |
| S91*/str/10 | 320 | 0 | 4 | 1,960 | 0 | -25 |
| S91*/off/50 | 1010 | 4 | 5 | 5,370 | 13 | -20 |
| SP98/off/10 | 174 | 2 | 0 | 900 | 12 | 0 |
| SP98/mod/10 | 158 | 3 | 0 | 860 | 18 | 0 |
| SP98/str/10 | 325 | 1 | 1 | 1,630 | 3 | -3 |
| SP98/off/50 | 988 | 5 | 7 | 4,910 | 19 | -24 |
| SP98r/str/10 | 356 | 4 | 0 | 2,030 | 18 | 0 |
| SP98r/off/50 | 1214 | 14 | 7 | 6,290 | 63 | -16 |
| RR/off/10 | 135 | 3 | 0 | 1,060 | 16 | 0 |
| RR/mod/10 | 119 | 3 | 0 | 1,000 | 9 | 0 |
| RR/str/10 | 315 | 9 | 0 | 1,820 | 30 | 0 |
| RR/off/50 | 1061 | 8 | 3 | 5,410 | 26 | -6 |

^aSee text for details on noninductive/inductive charging. Totals are shown for 130 minutes elapsed time from model initiation. The noninductive scheme is denoted by TAK [Takahashi, 1978], GZ [Ziegler et al., 1991], SP98 [Saunders and Peck, 1998], SP98r (see section 3.3.4.1), RR (Riming Rate), and S91 [Saunders et al., 1991]. Inductive charging strength is indicated by “off” (none), “mod” (moderate), or “str” (strong) and is followed by the minimum ice crystal concentration (units of L^{-1}).

settings of inductive charging are used: off, moderate (mod: $E_r = 0.007$ and $\langle \cos \theta \rangle = 0.2$), and strong (str: $E_r = 0.015$ and $\langle \cos \theta \rangle = 0.45$). The third sensitivity test looks at consequences of changing the specified minimum ice crystal concentration. As in HWF, the mass content is predicted for the ice crystal categories, leaving the size and concentration undetermined. The base model of HWF fixed the ice crystal radius at $10 \mu\text{m}$, so that concentration varied directly with mass content, up to a maximum of $1000 L^{-1}$, at which point the crystal size was increased. In the current model used here, the ice crystal concentration is diagnosed by estimating the number of activated ice nuclei [Meyers et al., 1992; Straka and Mansell, 2005], and for this study a maximum of $1000 L^{-1}$ was set for each of the three ice crystal categories. Both methods suffer from potential errors: The first method would overestimate concentration when the size should be larger, and the second method would underestimate concentration in situations where ice crystal multiplication processes are significant, especially at higher temperatures (-15°C to 0°C). To test the possible effects of underestimation, a set of simulations increased the minimum ice crystal concentration from $10 L^{-1}$ to $50 L^{-1}$. The actual crystal concentration at a point may be lower than the specified minimum because a constraint on the minimum ice crystal mass (6.88×10^{-13} kg) takes precedence. The changes to the minimum ice crystal concentration did not cause significant differences in the microphysical evolution, so that simulations with different minimum ice concentration are

fully comparable. In addition to the three main sensitivities, some further simulations examined changes specific to the SP98 and S91 noninductive charging schemes.

[47] A wide range of total lightning flashes among the cases is seen in Table 2. Two trends are evident within each noninductive scheme. One trend is the effect of inductive charging on the number of IC lightning flashes while holding the minimum ice crystal concentration to $10 L^{-1}$. There is a reduction in total IC flashes between off and moderate inductive charging, suggesting an overall mild discharging effect at the moderate setting. The strong (str) inductive charging enhances the net charge separation, resulting in more lightning flashes, almost double the number of total flashes, on average. A second trend is the increase in flashes as the minimum ice crystal concentration is increased. More numerous, smaller crystals tend to cause stronger electrification than fewer larger crystals, but the expectation might be the opposite since the parameterizations predict more separated charge per rebounding collision for larger crystals. When the charge dependence on crystal diameter is less than cubic, however, fewer, larger crystals separate less charge because the collision rate decreases faster than the increase in charge per collision for a fixed mass content of ice crystals. As it turns out, though, the main effect of changing the minimum concentration comes from the limits on charge separated per rebounding collision (20 fC for ice crystals) when the charge per rebounding collision for larger, less numerous crystals far exceeds the limit. For example, if one large crystal would separate 40 fC but is limited to 20 fC , two smaller crystals with half the mass might separate 20 fC each, effectively doubling the net separation rate.

5.1. TAK Results

[48] The three sensitivity tests with the TAK scheme had similar charge structures. Figure 7 shows that at 52 min the TAK simulations had a “normal” polarity charge structure consisting of a strong net negative charge region at 5 to 7 km altitude (higher in the updraft region) and strong net positive charge above 6 to 8 km. Positive charge also appeared beneath the strong negative region (the so-called lower positive charge or LPC) at altitudes below about 5 km ($-10^\circ\text{C} \leq T \leq 5^\circ\text{C}$). This arrangement of three significant charge layers is commonly referred to as the ‘normal tripole’ [Simpson and Scrase, 1937; Williams, 1989]. A thin negative charge screening layer at the top cloud boundary also developed due to the flux of negative ions toward the cloud top and their attachment to ice crystals.

[49] Noninductive charging rates at 52 min for the TAK scheme with low ice (TAK/10) are shown in Figure 7b. Graupel charged positively at higher temperatures or lower cloud water contents, and a large fraction of the charge separation occurs in regions where $CWC < 1.0 \text{ g m}^{-3}$. At -10° to -20°C , graupel gained negative charge in the updraft core where the CWC was higher, and the boundary between positive and negative charging followed roughly the edge of the 1 g m^{-3} contour of CWC. Positive noninductive charging rates were fairly low and produced a lower positive charge region (Figure 7a) that was too weak to initiate lightning.

[50] Strong inductive graupel-droplet charge separation had the effect of enhancing the main negative and positive

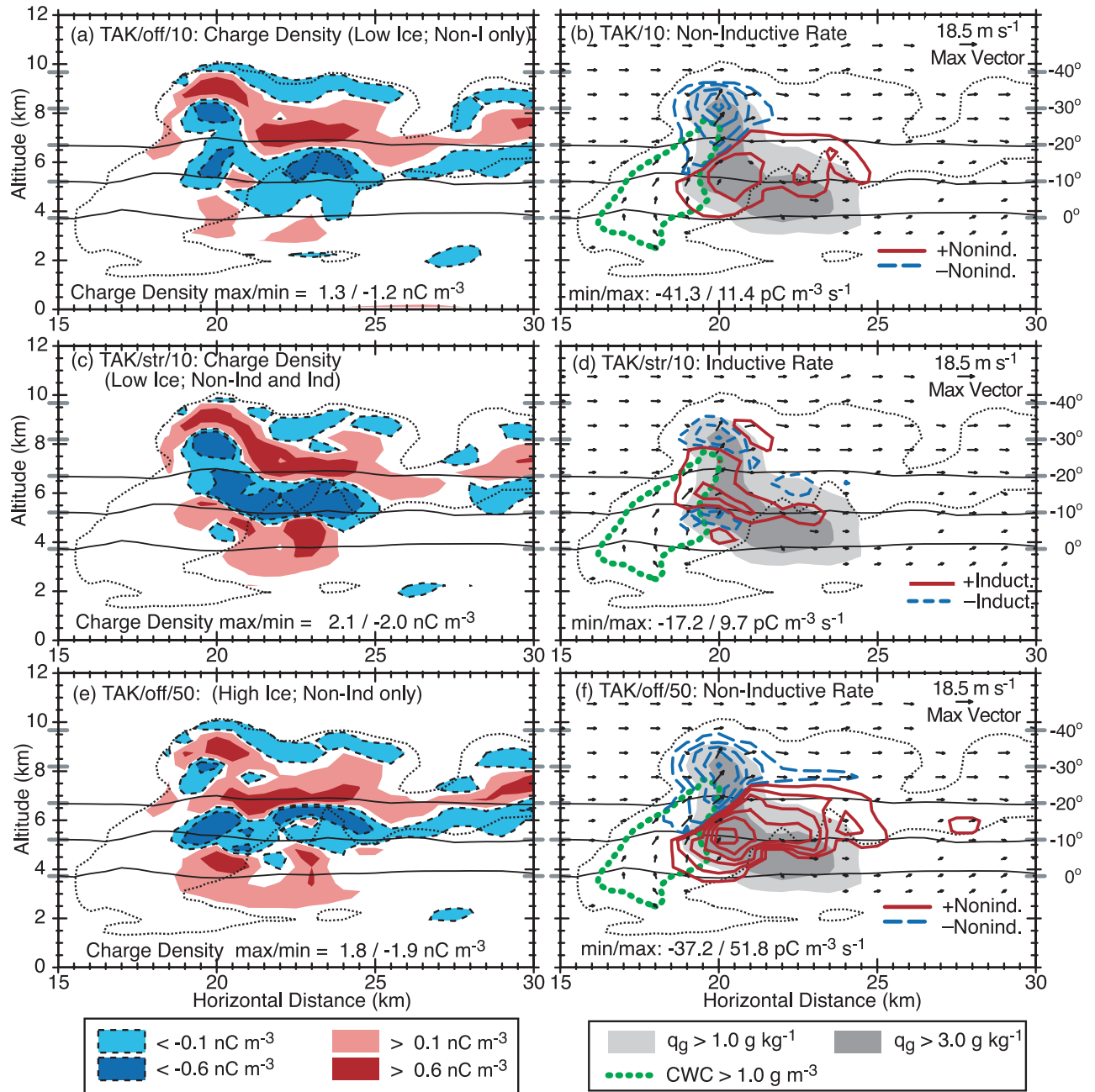


Figure 7. Charge structure (left) and charge separation rates (right) at 52 min from the TAK noninductive charging scheme. Cloud boundary (thin dotted line) and isotherms (thin horizontal lines at 0°, -10°, and -20°C) are the same in all panels. Left column: Net negative charge density (cyan, blue, dashed) and net positive charge (pink, red). Right column: Noninductive charge separation rates and inductive charging rates with contour intervals of ± 1 , ± 6 , and ± 15 $\text{pC m}^{-3} \text{s}^{-1}$ increasing thereafter by intervals of $10 \text{ pC m}^{-3} \text{s}^{-1}$ (negative and positive to graupel in blue-dashed and red). Note that the noninductive charging rates (b) apply to both (a) TAK/off/10 and (b) TAK/str/10. The green (heavy short dashed) contour in (b, d, and f) shows cloud water content of 1 g m^{-3} . Storm-relative wind vectors are shown at every second model point and only where the speed is greater than 5 m s^{-1} . Filled gray contours show total graupel mixing ratio (the sum of low, medium, and high density graupel). The wind vectors and graupel contours are the same in all similar plots.

charge regions (Figure 7c) and increasing the number of IC flashes (Table 2). The lower positive charge region was strengthened sufficiently to induce lightning, including -CG flashes. Contours of inductive charging rate (Figure 7d) reveal that induction enhanced the positive

charging of graupel near the -10°C level and higher in the updraft. The moderate level of inductive charging (not shown) also strengthened the LPC enough for a few -CG flashes. There was also a reduction in the number of IC flashes (from 181 to 154), but the dissipation of

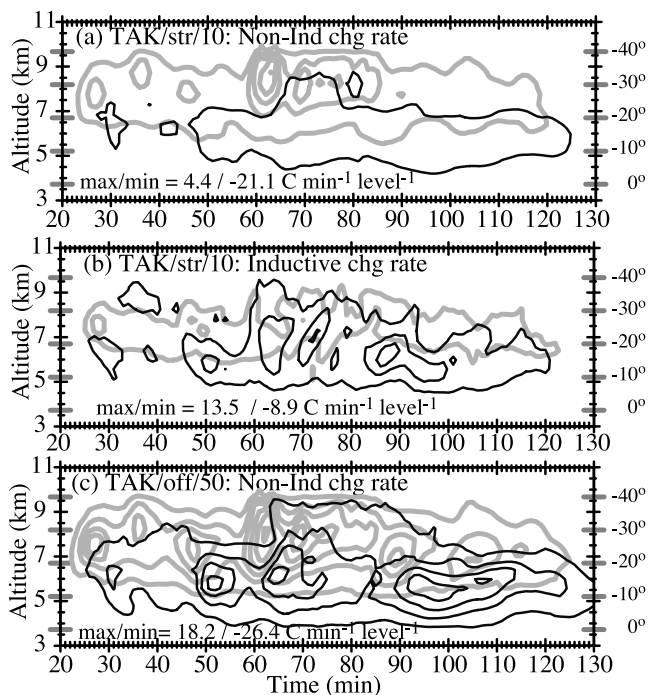


Figure 8. Horizontally integrated charge separation by graupel and hail per minute per model level for the TAK noninductive scheme. Contours of positive (thin black) and negative (thick gray) charging rates (per model level) with values of ± 1 , ± 5 , and $\pm 10 \text{ C min}^{-1} \text{ level}^{-1}$, with further constant increases of $\pm 5 \text{ C min}^{-1} \text{ level}^{-1}$.

energy by the $-CG$ flashes could have been partly responsible by leaving less energy for IC flashes.

[51] The LPC from the TAK scheme could also be enhanced significantly by increasing the minimum ice crystal concentration from 10 L^{-1} to 50 L^{-1} (Figure 7e). The increased ice concentration resulted in increasing the number of IC flashes nearly four-fold from the TAK/10/off case, but just over half the number of $-CG$ flashes as the case with strong inductive charging. A dramatic increase in positive charging of graupel is seen by comparing Figure 7d and Figure 7f, but an increase in negative charging is also evident from the larger area of the charging contours. A further test increasing the ice crystal concentration to 200 L^{-1} found another four to five-fold increase in IC flashes, but only about double the number of $-CG$ flashes.

[52] A more general picture of the charging rates produced by the TAK scheme and the accompanying inductive charging is given by the time-height plots in Figure 8. Negative noninductive charging rates were highest at altitudes of 7 to 10 km, while positive noninductive charging occurred mainly at 4 to 7 km (0° to -20°C). Positive charging at $T < -20^\circ\text{C}$ must have occurred in regions where $CWC < 0.3$ (Figure 1) because the maximum values of CWC at those altitudes (Figure 6d) were not large enough to reach the high-CWC positive charging zone. Inductive charging responded to the charge structure set up by the noninductive process and was most active in charging graupel positively at 5 to 8 km altitude. Increasing the minimum ice crystal concentration from 10 L^{-1} to 50 L^{-1} caused a respective increase in positive noninduc-

tive charging (Figures 8a and 8c) as well as a significant increase in negative noninductive charge separation.

5.2. GZ Results

[53] The GZ noninductive parameterization yielded results that were broadly comparable to the TAK scheme. A key difference between the GZ and TAK schemes is at lower temperature and cloud water content, where TAK has positive charging but GZ has negative charging. The TAK and GZ cases with lower ice concentration and strong inductive charging (str/10) had similar normal tripole (plus negative screening layer) charge structures at 52 min (Figure 7 and Figure 9). The first CG flash in the GZ/str/10 case was negative and initiated between the lower positive and main negative charge regions (Figure 9a) at 53 min.

[54] The time-height charging rates from the GZ scheme (Figure 10) were also similar to the TAK scheme results (Figure 8). A main difference of the GZ scheme was the strict altitude boundary between positive and negative charging that resulted from its simplified temperature dependence. The GZ scheme with $T_r = -15^\circ\text{C}$ had a shallower, weaker positive charging zone than TAK, which may explain the lower rate of $-CG$ flashes. The greater negative charging rates from the GZ scheme contributed to the higher total of IC flashes.

5.3. S91 Results

[55] The S91 noninductive scheme produced results similar to the GZ scheme but with half or fewer total lightning flashes. At the lower ice concentration setting of 10 L^{-1} with strong inductive charging (S91/str/10), the charge structure was quite similar to the GZ results at 52 min (Figures 9a and 9c). Unlike the GZ and TAK results, the S91 simulations started out with predominantly positive noninductive charging of graupel (Figures 11a, 11c, 11d, and 11e) due to high values of EW , resulting in an initial charge structure with negative charge above positive (negative dipole). This initial negative dipole was not significant enough to cause lightning, however, and, after a few minutes, most of the noninductive charging switched to negative.

[56] Sustained positive noninductive charging occurred at much lower temperatures ($T \leq -25^\circ\text{C}$) in the full S91 scheme results (Figures 11a and 11c) than in the TAK results (Figure 8). The PLEZ was the primary cause of this positive charging, although some of the positive charging occurred in conditions of sufficiently high EW . The role of the PLEZ was demonstrated by switching it off (S91*), causing the disappearance of the positive noninductive charging at $T < -25^\circ\text{C}$ (Figures 11d and 11e).

[57] The effect of the PLEZ charging can be seen in Figure 9d just outside of the main negative charging region (at 7 km altitude and 22 to 26 km horizontally). This positive charging zone did not substantially affect the charge structure in the low ice (10 L^{-1}) case. In the high ice concentration case of 50 L^{-1} , on the other hand, the positive charging was enhanced and resulted in a horizontal extension of the negative charge region at 7 to 8 km (not shown). Turning off the PLEZ resulted in a higher total number of IC flashes and greater total discharge by IC flashes (S91*; Table 2), suggesting that the PLEZ had, on average, a dissipating effect.

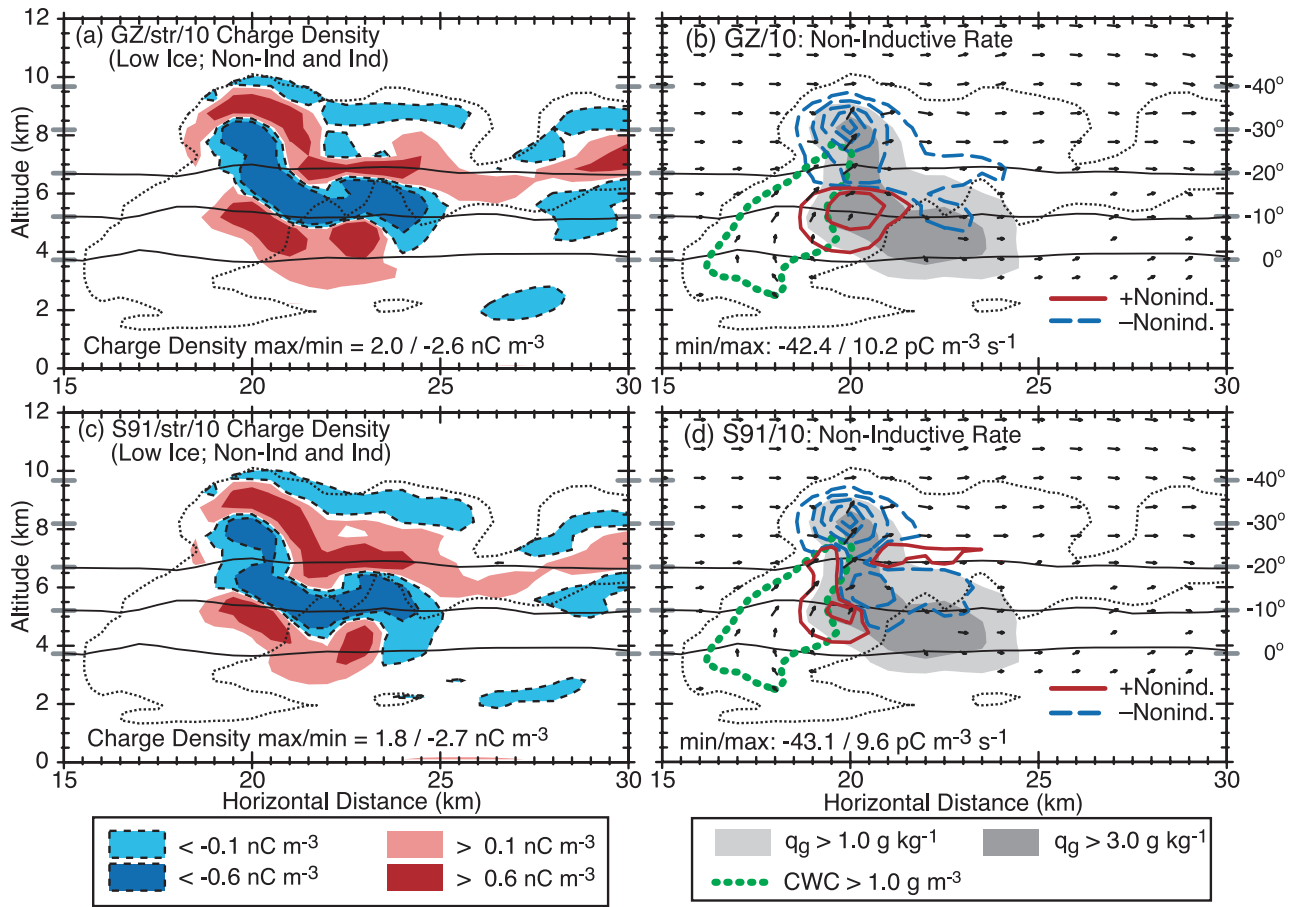


Figure 9. Charge structure at 52 min from GZ and S91 noninductive charge separation schemes. Right column: Noninductive charge separation rates (negative/positive to graupel in blue/red). Contour intervals as in Figure 7.

[58] Three of the S91 simulations produced +CG flashes (Table 2), similar to the GZ simulations. In each of these cases, the last CG flash was positive and occurred near the end of the simulation after 118 min. The two +CG flashes in the S91/off/10 and S91/str/10 cases happened within the time range of 116 to 119 min (Figure 16c). The CG flash activity was mostly unchanged when the PLEZ was turned off in the S91* cases. Although there were no +CG flashes for S91*/str/10, the downward trend for positive leaders at the end of the storm suggested that there was potential for one or more +CG flashes (not shown, but similar to Figure 16c).

5.4. SP98 and RR Results

[59] The results from SP98 and RR were comparable to each other, both producing a charge structure at 52 min (Figures 12a and 12c) that was nearly opposite to the TAK, GZ, and S91 results that included strong inductive charging. The updraft region exhibited an ‘inverted’ charge structure with a main positive charge region at $-30^{\circ}\text{C} < T < -20^{\circ}\text{C}$ (instead of negative) and an upper main negative charge and lower negative charge (instead of lower positive). An extra positive charge appeared in the updraft region below and to the side of the lower negative charge, but was lower and smaller in extent than in the TAK and GZ results. The vertical structure along a line through $x = 23$ km

(Figures 12a and 12c) was also the opposite of the other schemes (Figures 7 and 9).

[60] The cause of the inverted charge structure from the SP98 and RR schemes was clearly the greater amount of positive noninductive charging of graupel. The SP98 case showed positive charging throughout the full depth of the updraft (Figure 12b) at 52 min. The RR case had a higher RAR_{crit} than SP98, especially at low temperatures, and showed some negative charging at the top of the updraft (Figure 12d), but was still dominated by positive charging in the region shown at 52 min. The time-height charging plots (Figures 14b and 15b) show that inductive charging played a significant role in maintaining and enhancing the charge structure in the simulation.

[61] The primary difference between SP98 and RR appeared at low temperature (near -40°C). Comparing Figure 14a with Figure 15a, the RR scheme shifted the maximum positive charging rates to lower altitude during 60 to 65 min and eliminated the positive noninductive charging at about 9 km (-40° to -35°C) during the time period of 70 to 85 min. The SP98r variation, which assumed half the usual riming rate, switched much of the charging in the upper updraft region from positive to negative (compare Figure 12b with Figure 13b at 8–9 km and 60–65 min), while leaving some positive graupel charging at lower temperatures (Figure 14d). The SP98r/str/10 charge struc-

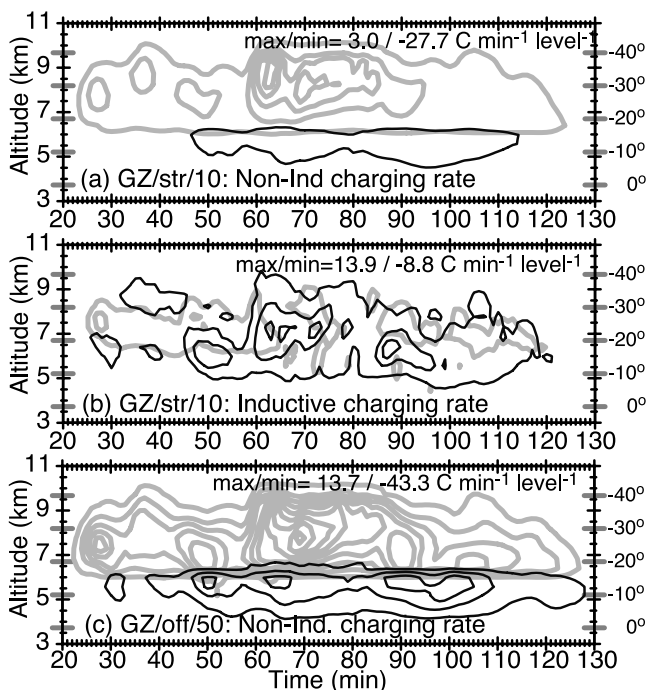


Figure 10. Horizontally integrated charge separation by graupel and hail per minute per model level for the GZ noninductive scheme. Contours of positive (thin black) and negative (thick gray) charging rates (per model level) with values of ± 1 , ± 5 , and $\pm 10 \text{ C min}^{-1} \text{ level}^{-1}$, with further constant increases of $\pm 5 \text{ C min}^{-1} \text{ level}^{-1}$. Panels (a) and (b) show noninductive and inductive charge separation rates for the low minimum ice case (10 L^{-1}), and panel (c) shows noninductive charge separation rates for the high minimum ice case (50 L^{-1}).

ture at 52 min (Figure 13a) looked more like the GZ and S91 results but with a smaller LPC.

[62] Increasing the minimum ice crystal concentration from 10 to 50 L^{-1} caused a greater overall increase in negative noninductive charging than in positive for each of the *RAR*-based schemes. Positive noninductive charging was a maximum at the early stage of new updraft pulses, and the storm switched to dominant negative charging as the cloud water contents and rime accretion rates decreased (Figures 14c, 14f, and 15c.) The greater increase in negative charging at mid and upper levels, combined with more positive noninductive charging at -10° to -20°C helped to revert the charge structure toward normal tripole structure. The SP98 and RR schemes produced significant numbers of $-CG$ flashes (three or more) only in the off/50 cases.

5.5. Lightning

[63] Figure 16 shows the time-height evolution of total lightning for simulations with the str/10 setting (strong induction and minimum 10 ice crystals per liter). Lightning responds to the charge structure and thus indicates the charge regions that are significant enough to be involved in a flash. Negative leaders (line contours) indicate ambient significant positive charge, and vice versa for positive channels (filled contours). The TAK, GZ, and S91 cases (Figures 16a, 16b, and 16c) had lightning that indicated an initial normal dipole charge (positive charge above nega-

tive), with later development of a significant LPC starting around 50 min and $-CG$ flashes. The lightning in SP98 and RR cases (Figures 16d and 16e), on the other hand, showed an initial inverted dipole charge structure. The RR case quickly added a significant lower negative region and associated $+CG$ flashes. A normal dipole was evident for the SP98r case (Figure 16f), though a significant upper negative region appeared at 35 to 45 min, composed of ice crystals charged negatively by noninductive charging. The SP98r lightning was more similar to the RR result than to SP98. Both the SP98r and RR cases showed stronger positive inductive charging than in the regular SP98 case at around -10 to -15°C starting at 90 min (Figures 14e and 15b), contributing to the conditions for subsequent $+CG$ flashes.

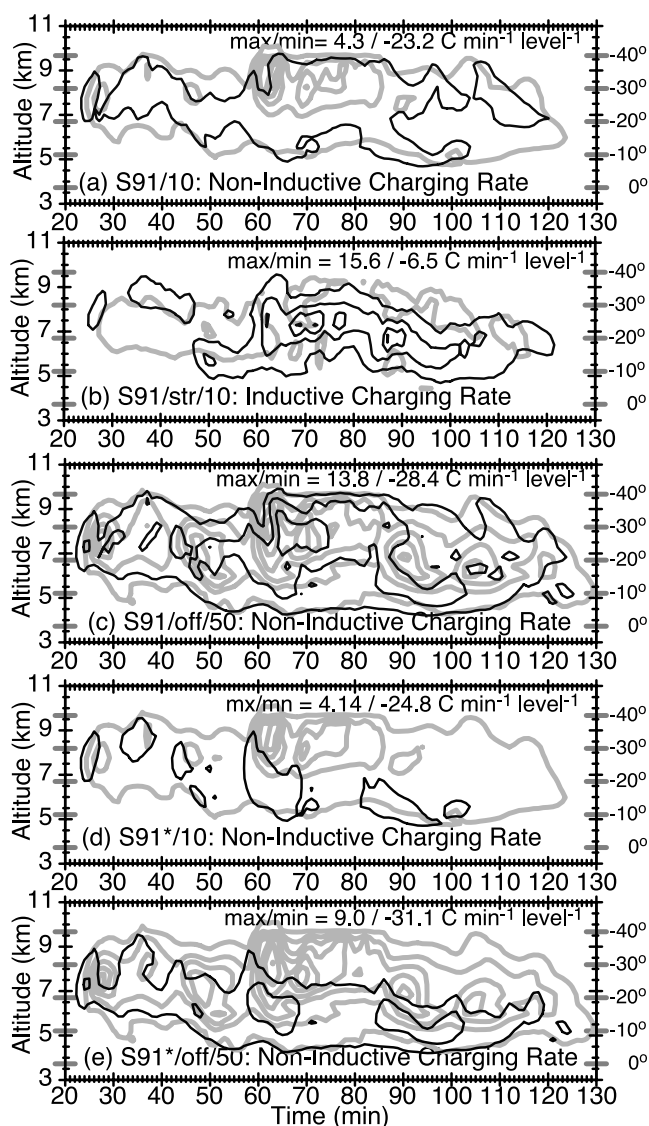


Figure 11. Horizontally integrated charge separation by graupel and hail per minute per model level for the S91 noninductive scheme. Contours of positive (thin black) and negative (thick gray) charging rates (per model level) with values of ± 1 , ± 5 , and $\pm 10 \text{ C min}^{-1} \text{ level}^{-1}$, with further constant increases of $\pm 5 \text{ C min}^{-1} \text{ level}^{-1}$.

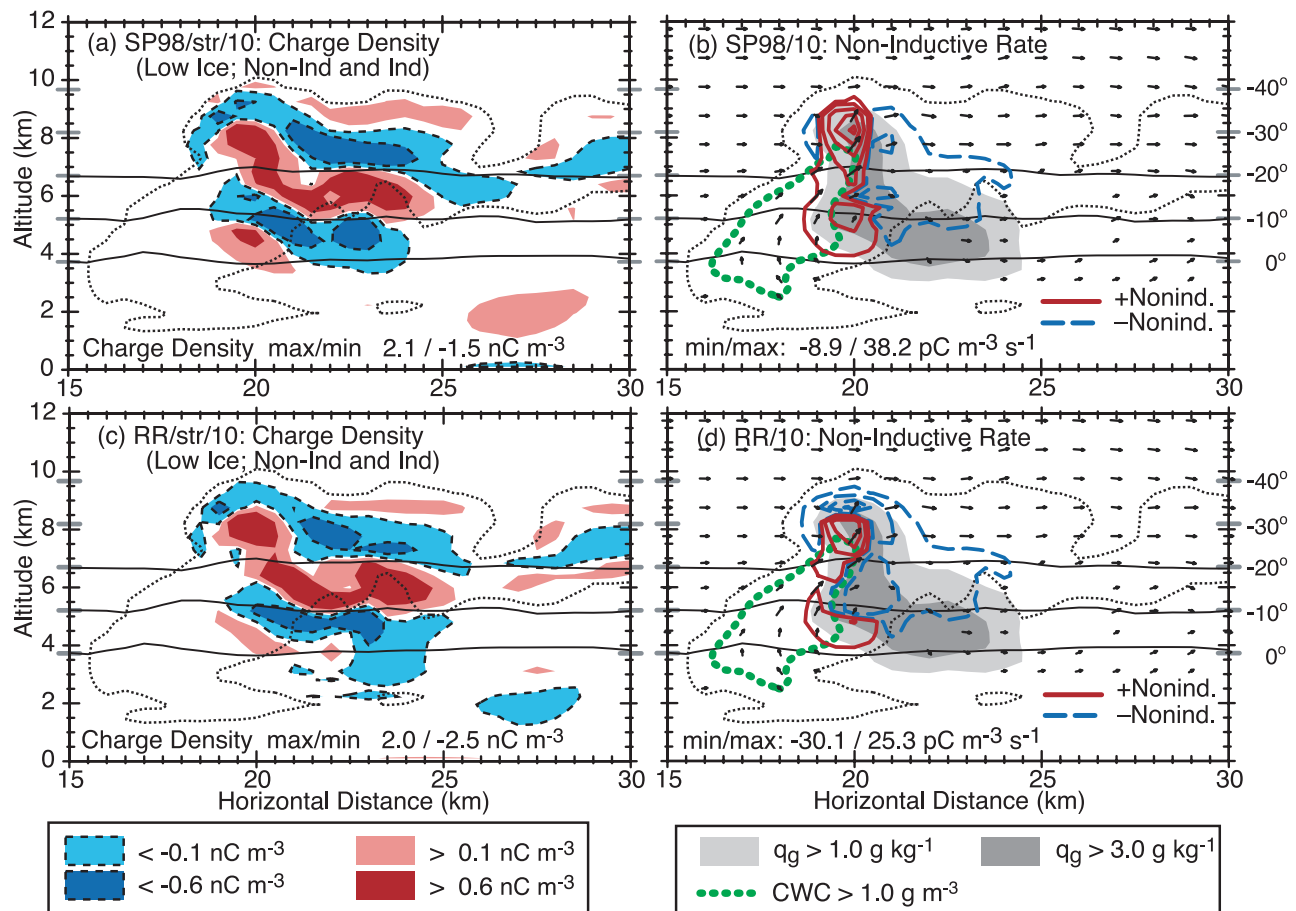


Figure 12. Charge structure at 52 min from the SP98 (a, b) and RR (c, d) noninductive charge separation schemes. Contour intervals as in Figure 7.

[64] One common feature of the lightning from each of the schemes is a correlation between the lightning and reflectivity heights. A comparison of the time-height maximum reflectivity (Figure 6a) and lightning (Figure 16) finds that each rise and fall in reflectivity height is mirrored in the lightning heights (e.g., at 40, 65, 80, and 105 min) as

has been observed in nature [e.g., *Krehbiel et al.*, 1984; *Lhermitte and Krehbiel*, 1979; *Lhermitte and Williams*, 1985; *Ushio et al.*, 2003].

[65] A number of simulated lightning flashes propagated far upward from the storm top, even reaching the top of the model domain (Figure 16). Although a lightning discharge

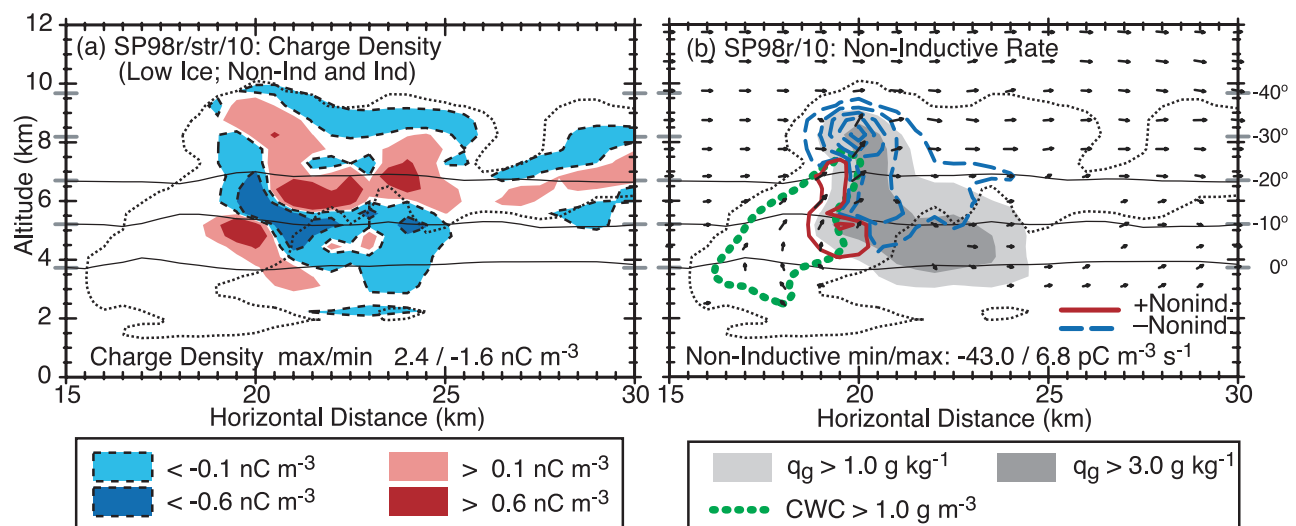


Figure 13. Charge structure at 52 min from the SP98r variation of the SP98 noninductive charge separation scheme. Contour intervals as in Figure 7.

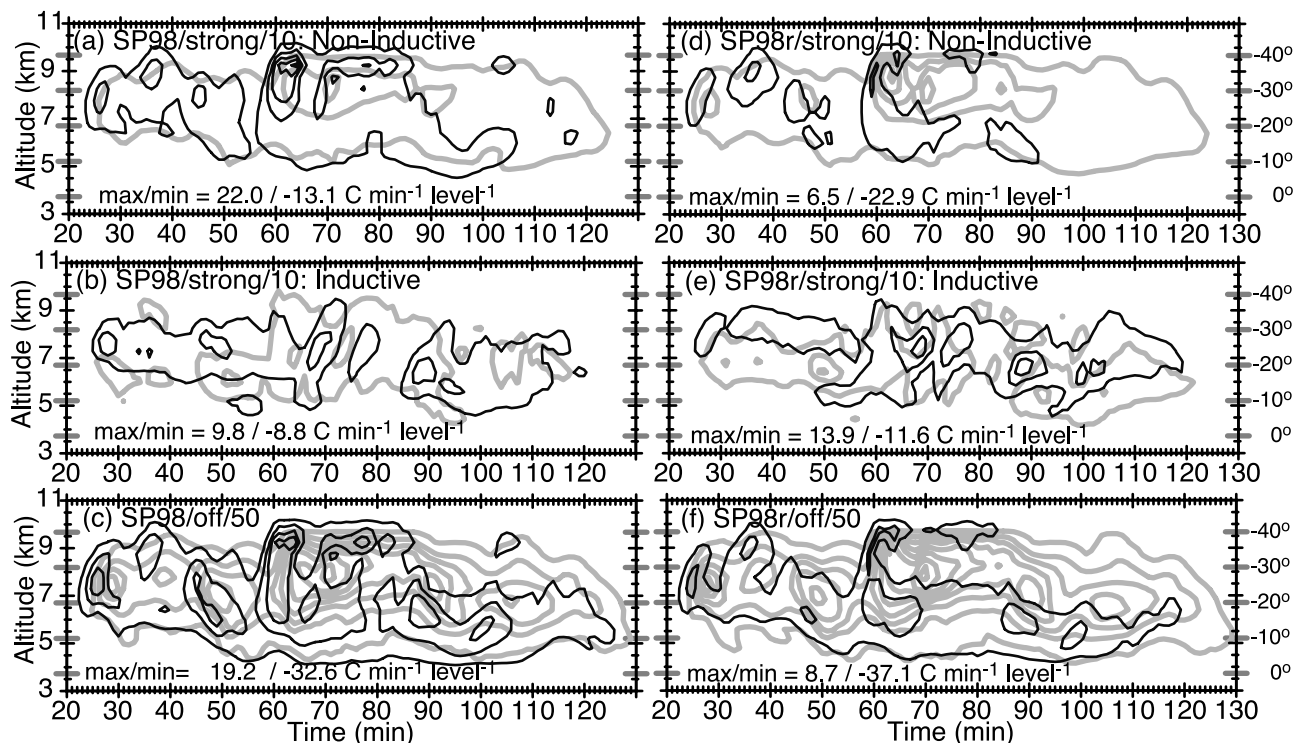


Figure 14. Horizontally integrated charge separation by graupel and hail per minute per model level for the SP98 noninductive scheme. Contours of positive (thin black) and negative (thick gray) charging rates (per model level) with values of ± 1 , ± 5 , and $\pm 10 \text{ C min}^{-1} \text{ level}^{-1}$, with further constant increases of $\pm 5 \text{ C min}^{-1} \text{ level}^{-1}$. Panels (a) and (b) show noninductive and inductive charge separation rates for the low minimum ice case (10 L^{-1}), and panel (c) shows noninductive charge separation rates for the high minimum ice case (50 L^{-1}). Panels (d–f) show the same quantities for the SP98r variation where the input value of RAR was halved.

from cloud to stratosphere was observed by *Pasko et al.* [2002], such flashes in the model appear to be primarily the result of numerical issues. Some improvements were made to the lightning parameterization after the completion of the simulations represented in Table 2. The improvements helped to maintain better charge neutrality during flash propagation and allowed for a lower electrical resistance. A few cases were rerun with the newer lightning scheme, and most of the above-cloud lightning activity was eliminated. Otherwise, the same general lightning behaviors were reproduced, with the conclusion that the results of the present study would not be adversely affected.

6. Discussion

6.1. Comparison With Previous Studies

[66] Only a few studies have attempted to compare noninductive charging from different laboratory results in multiple (two or three) dimensions. The work *Scavuzzo and Caranti* [1996] and *Scavuzzo et al.* [1998] was three dimensional and attempted to compare the laboratory results of *Takahashi* [1978] and *Saunders et al.* [1991]. These two studies were limited by the lack of coupled, predicted ice microphysics in their model. Instead, they took a warm-physics cloud and injected arbitrary vertical distributions of ice particles. That method ignored the charging history of particles and therefore effectively studies only charging rates over a short period of time. In terms of model

dynamics and microphysics, then, the only comparable multidimensional numerical charging sensitivity study is *Helsdon et al.* [2001] (HWF), whose tests included noninductive parameterizations based on *Takahashi* [1978] and *Saunders et al.* [1991].

[67] The HWF modeling case was the 19 July 1981 storm from the Cooperative Convective Precipitation Experiment (CCOPE). The CCOPE storm was similar to the present case in that both had precipitation development that was dominated by the ice process. The noninductive charging parameterizations in HWF for *Takahashi* [1978] and *Saunders et al.* [1991] are broadly similar for the TAK and S91 schemes without inductive charge separation (sections 3.3.1 and 3.3.3). One difference from the present study is that HWF did not include the factor α (12) for the Takahashi scheme. In the TAK results, the initial charge structure is a positive dipole and a negative electrical screening layer develops by ion attachment, as occurred in HWF. The positive charging of graupel at low cloud water content and low temperature (around -20°C) noted by HWF is also seen in the present results with the TAK scheme (Figure 7).

[68] The results using the S91 scheme had a similar early electrification as in HWF, where the charge structure initially developed as a negative dipole but then switched over into a positive dipole structure. In the present case, no lightning was produced by the initial negative dipole structure (e.g., Figure 16c), as in HWF, which had an

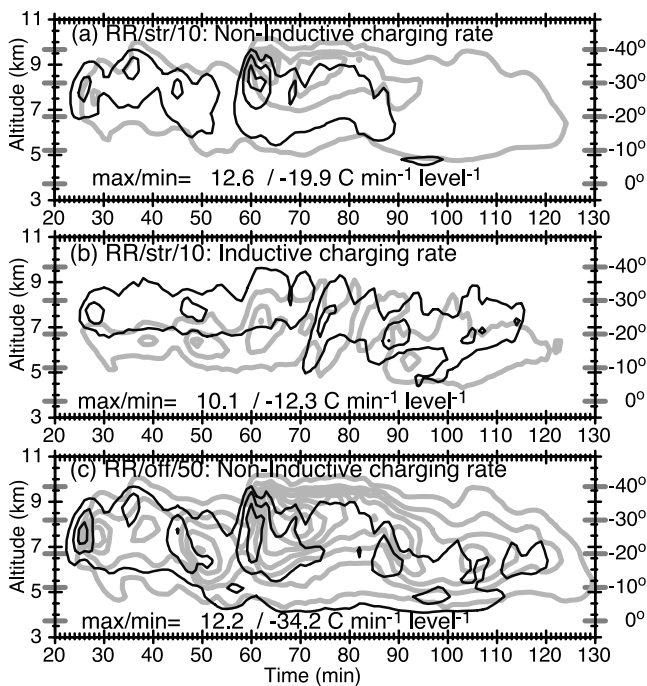


Figure 15. Horizontally integrated charge separation by graupel and hail per minute per model level for the RR noninductive scheme. Contours of positive (thin black) and negative (thick gray) charging rates (per model level) with values of ± 1 , ± 5 , and ± 10 $\text{C min}^{-1} \text{level}^{-1}$, with further constant increases of ± 5 $\text{C min}^{-1} \text{level}^{-1}$.

overall reduction in charging rate by a factor of 10. A similar reduction was not needed in the present case, perhaps because of the limit on charge separation of 20 pC per rebounding graupel-ice collision. No test with reduced *EW* was performed like the one done by HWF, but it is expected that it would also reduce the initial positive charging of graupel, similar to the effect seen in the SP98r variation of the SP98 scheme, which reduced the assumed rime accretion rate by half.

[69] The ‘1.5’ dimensional modeling study of *Solomon and Baker* [1998], which used only the *Saunders et al.* [1991] scheme, is worth mentioning. They also noted initially weak inverted electrification when higher concentrations of ice nuclei were available at higher temperatures, but otherwise normal-polarity electrification as *EW* decreased by freezing and riming and graupel rose higher in the updraft to lower temperature. The case was a New Mexico storm, which seems to be comparable to the storms in HWF and the present case.

6.2. Charge Structure and CG Flash Polarity

[70] The dominant model of typical thunderstorm charge structure has been the normal tripole [e.g., *Williams*, 1989] (or ‘normal quadrupole’ if a negative charge screening layer at cloud top is included). The TAK and GZ schemes consistently produced such a normal polarity charge structure (Figures 7b and 9a). The simulation with the S91 scheme also exhibited a normal tripole at the same time (Figure 9c). All three also had a negative screening charge layer at the upper cloud boundary. In the simulated tripole structure, $-CG$ flashes were initiated by the large electric

field magnitudes between the main negative and lower positive charge regions [e.g., *Clarence and Malan*, 1957; *Jacobson and Krider*, 1976; *Williams*, 1989]. The S91 cases also had a main positive charge above a main negative charge at the time of first lightning (Figure 16c).

[71] The RAR-based schemes (RR and SP98), resulted in ‘inverted’ polarity charge structure during the first hour or more of the simulation (e.g., as in Figure 12a). The inverted charge structure was reflected in the lightning activity, which showed negative channels in the -10°C to -20°C level with positive leaders above them, persisting through 70 min or more (Figures 16d and 16e). In the RR/str/10 case (Figure 16e), the lower negative charge region was significant enough to initiate IC and $+CG$ flashes, which is very much the opposite behavior of the TAK, GZ, and S91 results (Figures 16a and 16b). The lightning from the SP98/str/10 also indicated a strong lower negative charge, but no $+CG$ flashes until the end of the simulation. As previously noted in *Mansell et al.* [2002], $+CG$ flashes in the model always required a lower negative charge region for initiation, analogous to the role played by the lower positive charge for $-CG$ discharges, as suggested by observations [e.g., *Krehbiel et al.*, 2000].

[72] The model results for the TAK and SP98 schemes exhibited a stark difference in charge and lightning structure, at least during the first 70 to 90 min of the storm lifetime. After about 70 to 80 min, however, the lightning signatures tended to look similar across all the schemes, at least for the middle and upper altitudes (Figure 16). The RAR-based schemes tended to have mostly normal-polarity lightning by about 70 min, with the exception of the SP98, which maintained a significant upper negative charge layer (and positive lightning channels) until about 80 min. The switch to dominant normal polarity coincided with the decline in peak CWC (Figure 6d) and respective riming rates. The RAR-based schemes also did not show much significant lower positive charge, in contrast to TAK, GZ, and S91, in terms of involvement with lightning.

[73] Near the end of the storm (115 to 130 min), only the TAK result had a lower positive charge that was still involved in lightning. The TAK result maintained a relatively constant lower cut-off to positive leaders, in contrast to the others, which tended to show positive leaders reaching to lower altitudes in the last few minutes of activity, usually including a $+CG$ flash. These end-of-storm $+CG$ flashes occurred as the last active cell decayed and negatively-charged graupel descended closer to ground. In the TAK scheme, however, graupel receives positive charge at lower values of CWC and temperatures of 0° to -20°C and for any value of CWC at $T > -10^{\circ}\text{C}$ (Figure 1). As a result, graupel that fell out of the storm through a region of low CWC tended to acquire positive charge (or become less negatively charged) in the TAK scheme, where the other noninductive schemes more likely to indicate negative charging (e.g., compare the region $X > 22$ km and $T > -20^{\circ}\text{C}$ in Figure 7b for TAK and Figure 9d for S91).

6.3. Role of Inductive Charging

[74] The model results suggest that conditions may exist under which inductive graupel-droplet charging might be an important secondary electrification effect. A test with only ‘‘strong’’ inductive charging yielded electric fields barely

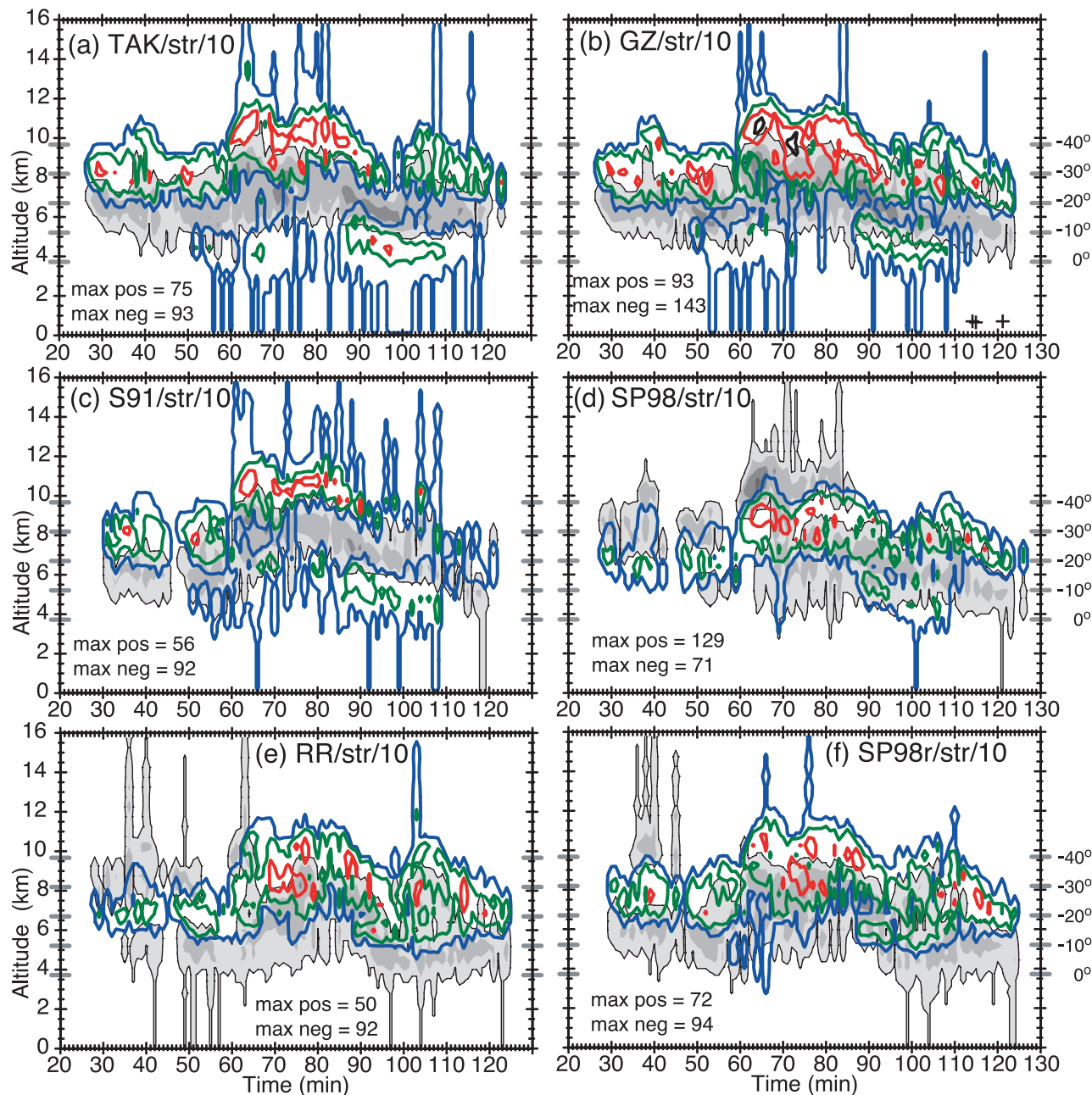


Figure 16. Time-height representation of lightning activity. Positive and negative leader segments were added up over each model level on 1 min intervals. Gray-filled contours indicate positive leader segments, colored line contours show negative leader segments, and both have values of 0.75, 10, 40, and 100 segments per level (blue, green, red, and black, respectively). (a) *Takahashi* [1978] (TAK), (b) *Gardiner-Ziegler* (GZ), (c) *Saunders et al.* [1991] (S91), (d) *Saunders and Peck* [1998] (SP98), (e) *Riming Rate* (RR), and (f) SP98r (SP98 with doubled RAR_{crit}). All cases had low ice ($10 L^{-1}$) and strong inductive charging (str/10). The “+” symbols in (b) indicate when +CG flashes occurred at the end of the storm in the other GZ cases.

larger than the fair-weather field (not shown), consistent with the model results of *Helsdon et al.* [2002], indicating that noninductive charge separation is the primary mechanism in the model and is required to generate fields large enough to make polarization charging significant. The lower-efficiency “moderate” inductive charging parameters led to slightly weaker overall electrification as measured by total discharge (Table 2). When the “strong” inductive charging parameters

were used, however, the overall electrification was significantly increased. For the TAK, GZ, and S91 schemes, (minimum ice crystal concentration of $10 L^{-1}$) inductive charging was important for the development of a lower positive charge region (and enhanced main negative charge region), resulting in –CG flashes.

[75] When a larger minimum ice crystal concentration is assumed, however, the model results suggest that nonin-

ductive graupel-ice charging by itself could be capable of producing significant lower-altitude charge regions under the right conditions. This result indicates the importance of determining the ice crystal concentration in the temperature range of 0° to -15°C . The use of constant value for droplet concentration may tend to exaggerate the effect of inductive charging at mid and upper altitudes, where actual droplet concentrations might be lower because of accretion and parcel expansion. The inductive charging equation (27) essentially has an inverse dependence on droplet diameter (i.e., D^{-1}) as size and concentration are varied for the same CWC. Thus the effect of inductive charging is expected to decrease as the droplet size increases and number concentration decreases for a constant droplet mass content. Clearly, prediction of droplet and crystals concentrations will be needed for further model investigations of charge separation at higher temperatures.

6.4. Delay of CG Flashes

[76] All of the lightning histories in Figure 16 show a delay of 15 minutes or more from the time of the first IC flash to the first CG flash. By about 50 minutes, the TAK, GZ, and S91 cases had developed a lower positive charge that is involved in IC and $-$ CG flashes, coincident with growth in graupel mass at lower levels (Figure 6c). The inverted charge structure early in the SP98 case has similar timing for a few IC flashes involved in a lower negative charge region, but no CG flashes.

[77] The charge development at lower altitudes is a consequence of the precipitation-based charging mechanisms as graupel reaches and builds at lower altitudes in the storm cells. As described in section 4, the simulated storm develops precipitation exclusively by the ice process, so the initial development of graupel is high in the storm, and the graupel falls out downstream of the updraft. Some of the graupel (still frozen or melted) is entrained back into updraft, where it can (refreeze and) resume riming and be active in generating the lower charge regions (either by noninductive or inductive mechanisms), which may then initiate CG flashes. The result is a substantial delay between the first IC and CG flashes [Workman and Reynolds, 1949; Lhermitte and Krehbiel, 1979; Goodman et al., 1988; Williams et al., 1989]. A similar development process was seen in the axisymmetric wintertime (cold cloud base) maritime cloud simulation of Takahashi [1984], where graupel was the dominant form of precipitation. In that case, however, the graupel fell back down through the updraft rather than being entrained, because the model could not have environmental wind shear.

7. Summary and Conclusions

[78] The primary goal of this study was to demonstrate the charging behavior from parameterizations of different laboratory studies in the context of a numerical storm simulation. In the chosen continental multicellular storm, the TAK, GZ, and S91 schemes produced normal-polarity storms and $-$ CG flashes, whereas the RAR-based schemes (SP98 and RR) had initially inverted-polarity charge structure. When the graupel collection efficiency was assumed to be 0.5 instead of nearly 1.0, the SP98r scheme acted much like S91. The S91 and SP98r schemes did produce an

initially inverted charge structure (positively charged graupel), but it was too weak to initiate lightning. The model results support the primary role of noninductive charge separation for thunderstorm electrification and allow a secondary and possibly important role for inductive charge separation by rebounding graupel-droplet collisions. The model only treats this one form of inductive charging, however, and other inductive mechanisms might be important, such as inductive separation through drop break-up or liquid shedding from melting ice.

[79] Recent observations from the Severe Thunderstorm Electrification and Precipitation Study (STEPS) [Lang et al., 2004] with lightning mapping [e.g., Krehbiel et al., 2000] and in situ electric field soundings [Rust and MacGorman, 2002] have revealed that many storms in the western-Kansas eastern Colorado region appeared to have an inverted charge structure. These observations raise the question whether any of the noninductive charge separation schemes could cause inverted polarity storms. The GZ scheme is unlikely to produce inverted polarity unless the reversal temperature were set very low [e.g., Ziegler et al., 1991]. The TAK and S91 schemes allow for positive charging of graupel at lower temperature for high values of CWC or *EW*. Sufficiently high *EW* for positive charging by S91 was reached in the multicell storm simulation, but it was insufficient to cause a significant or sustained inverted polarity charge structure. The high CWC threshold for positive charging at lower temperature in the TAK scheme was never achieved, although there was positive charging at lower temperatures with low CWC. Although peak values of CWC greater than 3 g m^{-3} occurred, they were confined to precipitation-free updrafts, where there was insufficient graupel for appreciable charge separation. When graupel does appear in the updraft, the CWC is rapidly reduced by scavenging.

[80] The SP98 and RR schemes, on the other hand, reached their positive charging regions much more easily with sustained high rime accretion rates. The model study thus suggests that the RAR-based schemes are more likely to be able to produce an inverted-polarity storm than the others. The SP98r result suggests that the SP98 scheme also could produce a normal-polarity storm with somewhat lower values of CWC or lower droplet collection efficiency. Even though the SP98 and RR schemes had much more positive charge gained by graupel than the other schemes at temperatures less than -20° , total negative charging was still greater than total positive charging. Each pulse of positive charging was followed by negative charging as riming reduced the CWC and in turn reduced the riming rates, which favored negative charging of graupel. Since the schemes based on rime accretion rate are more sensitive to the microphysical conditions, they appear also to be more versatile in the possible charge structures they can produce.

[81] Modeling results are necessarily dependent on the treatment of microphysical processes, and this study found sensitivities to ice crystal concentration and rime accretion rate, indicating aspects of the model microphysics that could be improved. The addition of number concentration prediction for droplets and ice crystals is in progress and will help the investigation of the effectiveness of noninductive charge separation at higher temperatures (-10 to 0°C). An enhanced microphysics scheme is not yet fully imple-

mented, but some initial tests suggest that ice crystal concentrations at higher temperatures could be large enough to generate lower charge regions without any action by inductive charging. These preliminary results would agree with the current results with minimum ice concentration of 50 L^{-1} and no inductive charging.

[82] Even as models become more sophisticated, however, there is still a great need for further laboratory studies, as there is much that is poorly understood that cannot be addressed by numerical models alone. For example, there is the question of the best ways to represent a mixed-phase cloud in a laboratory experiment. *Pereyra et al.* [2000] found that the technique for introducing ice crystals into a cloud chamber, either grown within the cloud (one-cloud method) or in a separate chamber (two-cloud method), can dramatically affect the results, especially at lower cloud water content. Another unanswered question is the effectiveness of noninductive charge separation in the lower temperature regime of -30 to -40°C . All of the simulations showed significant charge separation in that temperature range, where the charging parameterizations must rely on extrapolations of the laboratory data. The dependence of charge separation on the droplet size spectrum may also be important [e.g., *Jayarathne and Saunders, 1985; Avila et al., 1998; Avila and Pereyra, 2000*] for noninductive charging and deserves greater attention. Model parameterizations could also be improved by a better understanding of the effect of graupel particle temperature on charging. An investigation of charge separation between different-sized graupel particles or between graupel and aggregates (rather than single crystals) could also fill gaps in our understanding. For example, *Avila et al.* [2005] found that a target gained positive charge from larger irregular ice particles under conditions in which smaller crystals imparted negative charge. As insights on the microscale come out of new laboratory studies, electrification modeling will continue to investigate the possible consequences on the macroscale.

Appendix A: Small Ion Parameterization

[83] The model includes an explicit treatment of small ions, which are assumed to be singly charged. The conservation equation for positive and negative ion concentrations (n_+ and n_-) is

$$\frac{\partial n_{\pm}}{\partial t} = -\nabla \cdot (n_{\pm} \mathbf{V} \pm n_{\pm} \mu_{\pm} \mathbf{E} - K_m \nabla n_{\pm}) + G - \alpha n_+ n_- - S_{\text{att}} + S_{\text{pd}} + S_{\text{evap}} \quad (\text{A1})$$

[84] The first and third terms in parentheses are advection and turbulent mixing and are treated the same as for the other scalar variables. The second term, the ion drift motion, is treated similarly to the advection term with a sixth-order flux-form Crowley scheme [*Tremback et al., 1987*] with monotonic filter [*Leonard, 1991*]; G is the background cosmic ray ion generation rate; $\alpha n_+ n_-$ is the ion recombination rate; and the last three terms are ion attachment to hydrometeors (sink), point discharge current from the surface (source), and release of any charge as ions from hydrometeors that evaporate completely (source). If the ion drift speeds exceed the maximum for stable transport, then the ion processes (except advection and turbulent mixing)

are performed on a subdivided time step, leaving the dynamical time step unchanged. In practice this subdivision rarely occurs because the electric field values are limited according to the breakeven field threshold, which is smaller at higher altitudes and compensates for the increased ion mobilities.

[85] The fair weather state is defined as in *Gish* [1944] with the modified coefficients of *Helsdon and Farley* [1987]:

$$E_{z,\text{FW}} = E_0(b_1 e^{-a_1 z} + b_2 e^{-a_2 z} + b_3 e^{-a_3 z}) \quad (\text{A2})$$

where $E_0 = -80.0 \text{ V m}^{-1}$, $b_1 = 0.5$, $a_1 = 4.5 \times 10^{-3}$, $b_2 = 0.65$, $a_2 = 3.8 \times 10^{-4}$, $b_3 = 0.1$, $a_3 = 1.0 \times 10^{-4}$.

[86] At steady state in a fair-weather condition, the vertical positive and negative ion fluxes are

$$\frac{d}{dz} (n_+ \mu_+ E_{z,\text{FW}}) = G(z) - \alpha n_+ n_- \quad (\text{A3})$$

$$-\frac{d}{dz} (n_- \mu_- E_{z,\text{FW}}) = G(z) - \alpha n_+ n_- \quad (\text{A4})$$

where $G(z)$ is the ion generation rate by cosmic rays (held constant as a function of altitude), and $\alpha = 1.6 \times 10^{-12} \text{ m}^{-3} \text{ s}$ is the ionic recombination coefficient [*Chiu, 1978*].

[87] The ion mobilities μ are adopted from *Shreve* [1970]:

$$\mu_{\pm} = \beta_{\pm} e^{1.4 \times 10^{-4} z} \quad (\text{A5})$$

where $\beta_+ = 1.4 \times 10^{-4}$ and $\beta_- = 1.9 \times 10^{-4}$ and z is in meters. Diffusivity is derived from mobility by the Einstein relation

$$D_{\pm} = \frac{kT}{e} \mu_{\pm} \quad (\text{A6})$$

where k is Boltzmann's constant, T is the temperature (Kelvin), and e is the electron charge magnitude. (Note that μ_{\pm} includes an implicit factor of e .)

[88] Under steady-state (i.e., fair weather) conditions, we assume that the ion currents vary negligibly from constant, so that $\nabla \cdot \mathbf{j}_{\pm} = 0$. Therefore, from equation (A3) we get

$$G(z) = \alpha n_+ n_- \quad (\text{steady state}) \quad (\text{A7})$$

(as in *Takahashi* [1979]) and the cosmic ray generation rate is held constant in time throughout a simulation.

[89] Ion attachment to hydrometeors is a combination of diffusion, S_{diff} , and conduction, S_{cond} . As in *Chiu* [1978], the two terms are calculated separately and added ($S_{\text{att}} = S_{\text{diff}} + S_{\text{cond}}$). The equations for attachment by conduction are the same as found in *Chiu* [1978] (based on *Whipple and Chalmers* [1944]) and are not reproduced here. As in *Chiu* [1978], the vertical component of the electric field is used to calculate S_{cond} . The equation for diffusion attachment is similar to *Chiu* [1978]:

$$S_{\text{diff}\pm} = \frac{\partial n_{\pm}}{\partial t} \Big|_{\text{diff}} = \sum_j 4\pi r_j D_{\pm} n_{\pm} c_j f(X_j) \left[1 - \frac{r_j V_{Tj}}{2\pi D_{\pm}} \right] \quad (\text{A8})$$

where r_j , V_{Tj} , and c_j are the mean radius, mean terminal fall speed, and number concentration of the j th hydrometeor category. The factor $f(X_j)$ is from *Helsdon* [1980]:

$$f(X_j) = \frac{X_j}{e^{X_j} - 1} \quad (\text{A9})$$

where $X_j = Q_j/Q_D$; Q_j is the charge per particle in hydrometeor category j ; and $Q_D = 4 \pi \epsilon r_j k_B T/e$ is the hydrometeor charge at which the electric potential and thermal energies are balanced at the surface. In *Helsdon* [1980], X_j was allowed to become negative, which enhances diffusion for ions of opposite charge [i.e., $f(X_j) > 1$]. Here, we only allow positive values of X_j [i.e., $f(X_j) \leq 1$] to avoid the possibility of double-counting the ion attachment by conduction [*Chiu*, 1978].

[90] A point ion discharge current j_{pd} (corona current) is allowed when the vertical electric field component at the ground level exceeds a given threshold ($|E_z| > E_0$). The formulation used here follows *Jhawar and Chalmers* [1967] with values of *Standler and Winn* [1979]:

$$j_{pd} = CE_z(|E_z| - E_0)^2 \quad (\text{A10})$$

where $C = 2 \times 10^{-20} \text{ A m V}^{-3}$, and $E_0 = 5 \times 10^3 \text{ V m}^{-1}$, and E_z is the vertical electric field component at the ground. The discharge current j_{pd} is converted to an ion concentration rate $S_{pd\pm}$ as

$$S_{pd\pm} = \frac{j_{pd}}{q_e \Delta z} \quad (\text{A11})$$

where q_e is the electron charge magnitude and Δz is the vertical grid spacing at the first scalar grid point above ground. Note that $S_{pd+} = 0$ for $E_z < E_0$ and $S_{pd-} = 0$ for $E_z > -E_0$.

[91] In practice, the surface electric fields rarely exceed 15 kV m^{-1} except as a response to the charge deposited by CG flashes. When the E_z exceeds $15\text{--}20 \text{ kV m}^{-1}$, the cubic formulation begins to overpredict the average point discharge for a typical model time step of 3 to 5 s and thus can cause an overshoot in the ion density. A much smaller time step [e.g., *Standler and Winn*, 1979] would allow the initial large discharge rates to feed back quickly to limit further corona. Limiting the magnitude of E_z to 15 kV m^{-1} in (A10) still allows the modeled surface electric field to recover from large impulses (over 30 kV m^{-1}) within 2 model time steps (6 to 10 s). Additionally, a check is performed to ensure that the amount of corona charge is limited to that which just reduces the surface field back down to the threshold (cut-off) value.

[92] The boundary conditions for ions are specified on all domain boundaries. Ion concentrations at the top and lateral boundaries are not changed by drift motions (i.e., by ion currents). The normal electric field component is not necessarily zero at the lateral boundaries because the electric field is calculated in an extended domain (wider and taller) as described in section 3.2. Ion concentrations at the top of the cloud domain are held constant. The ion concentrations at the lateral boundaries can be affected by advection under outflow conditions but not by inflow, which is the case for advection of all scalar variables. Through the action of

vertical ion drift, boundary values return to fair-weather values following the passage of clouds through a boundary. Ion drift currents can bring charge into the domain through all boundaries.

[93] **Acknowledgments.** Support for this research was provided under National Science Foundation grants ATM-0119398, ATM-9617318, ATM-9807179, and ATM-003867. Additional support was provided through Office of Naval Research (ONR) grant N00014-00-1-0525. Funding for this research also was provided under NOAA-OU Cooperative Agreement NA17RJ1227. Thanks to K. Kuhlman for helping to find problems in the electrification code. Thanks also to R. Brown for feedback on the manuscript and to M. Gilmore for helpful discussions. The comments and suggestions of E. R. Williams and C. P. R. Saunders are also gratefully acknowledged.

References

- Adams, J. (1989), MUDPACK: Multigrid fortran software for the efficient solution of linear elliptic partial differential equations, *Appl. Math. Comput.*, *34*, 113–146.
- Aufdermaur, A. N., and D. A. Johnson (1972), Charge separation due to riming in an electric field, *Q. J. R. Meteorol. Soc.*, *98*, 369–382.
- Avila, E. E., and R. G. Pereyra (2000), Charge transfer during crystal-graupel collisions for two different cloud droplet size distributions, *Geophys. Res. Lett.*, *27*(23), 3837–3840.
- Avila, E. E., G. M. Caranti, N. E. Castellano, and C. P. R. Saunders (1998), Laboratory studies of the influence of cloud droplet size on charge transfer during crystal-graupel collisions, *J. Geophys. Res.*, *103*, 8985–8996.
- Avila, E. E., C. P. R. Saunders, H. Bax-Norman, and N. E. Castellano (2005), Charge sign reversal in irregular ice particle-graupel collision, *Geophys. Res. Lett.*, *32*, L01801, doi:10.1029/2004GL020761.
- Baker, B., M. B. Baker, E. R. Jayaratne, J. Latham, and C. P. R. Saunders (1987), The influence of diffusional growth rates on the charge transfer accompanying rebounding collisions between ice crystals and soft hailstones, *Q. J. R. Meteorol. Soc.*, *113*, 1193–1215.
- Baker, M. B., and J. G. Dash (1994), Mechanism of charge transfer between colliding ice particles in thunderstorms, *J. Geophys. Res.*, *99*(D5), 10,621–10,626.
- Brooks, I. M., and C. P. R. Saunders (1994), An experimental investigation of the inductive mechanism of thunderstorm electrification, *J. Geophys. Res.*, *99*, 10,627–10,632.
- Brooks, I. M., and C. P. R. Saunders (1995), Thunderstorm charging: Laboratory experiments clarified, *Atmos. Res.*, *39*, 263–273.
- Brooks, I. M., C. P. R. Saunders, R. P. Mitzeva, and S. L. Peck (1997), The effect on thunderstorm charging of the rate of rime accretion by graupel, *Atmos. Res.*, *43*, 277–295.
- Brown, R. A., and R. J. Meitin (1994), Evolution and morphology of two splitting thunderstorms with dominant left-moving members, *Mon. Weather Rev.*, *122*(9), 2052–2067.
- Carpenter, R. L., K. K. Droegemeier, and A. M. Blyth (1998), Entrainment and detrainment in numerically simulated cumulus congestus clouds, Part I: General results, *J. Atmos. Sci.*, *55*, 3417–3432.
- Chiu, C.-S. (1978), Numerical study of cloud electrification in an axisymmetric, time-dependent cloud model, *J. Geophys. Res.*, *83*, 5025–5049.
- Clarence, N. D., and D. J. Malan (1957), Preliminary discharge processes in lightning flashes to ground, *Q. J. R. Meteorol. Soc.*, *83*, 161–172.
- Cotton, W. R., G. J. Tripoli, R. M. Rauber, and E. A. Mulvihill (1986), Numerical simulation of the effects of varying ice crystal nucleation rates and aggregation processes on orographic snowfall, *J. Clim. Appl. Meteorol.*, *25*, 1658–1680.
- Deardorff, J. W. (1980), Stratocumulus-capped mixed layers derived from a three-dimensional model, *Boundary Layer Meteorol.*, *18*, 495–527.
- Dye, J. E., C. A. Knight, V. Toutenhoofd, and T. W. Cannon (1974), The mechanism of precipitation formation in northeastern Colorado cumulus III. Coordinated microphysical and radar observations and summary, *J. Atmos. Sci.*, *31*, 2152–2159.
- Foote, G. B., and H. W. Frank (1983), Case study of a hailstorm in Colorado. Part III: Airflow from triple-doppler measurements, *J. Atmos. Sci.*, *40*, 686–707.
- Gardiner, B., D. Lamb, R. L. Pitter, J. Hallett, and C. P. R. Saunders (1985), Measurements of initial potential gradient and particle charges in a Montana summer thunderstorm, *J. Geophys. Res.*, *90*, 6079–6086.
- Gaskell, W. (1981), A laboratory study of the inductive theory of thunderstorm electrification, *Q. J. R. Meteorol. Soc.*, *107*, 955–966.
- Gish, O. H. (1944), Evaluation and interpretation of the columnar resistance of the atmosphere, *Terr. Magn. Atmos. Electr.*, *49*, 159–168.

- Goodman, S. J., D. E. Buechler, P. D. Wright, and W. D. Rust (1988), Lightning and precipitation history of a microburst-producing storm, *Geophys. Res. Lett.*, *15*(11), 1185–1188.
- Grenet, G. (1947), Essai d'explication de la charge électrique des nuages d'orages, *Ann. Géophys.*, *3*, 306–307.
- Grenet, G. (1993), Possible explanation for the electric charge in thunderclouds (Reprint of 1947 paper in English), *Atmos. Res.*, *30*, 175–179.
- Helsdon, J. H., Jr. (1980), Chaff seeding effects in a dynamical-electrical cloud model, *J. Appl. Meteorol.*, *19*, 1101–1125.
- Helsdon, J. H., Jr., and R. D. Farley (1987), A numerical modeling study of a Montana thunderstorm: 2. Model results versus observations involving electrical aspects, *J. Geophys. Res.*, *92*, 5661–5675.
- Helsdon, J. H., Jr., W. A. Wojcik, and R. D. Farley (2001), An examination of thunderstorm-charging mechanisms using a two-dimensional storm electrification model, *J. Geophys. Res.*, *106*, 1165–1192.
- Helsdon, J. H., Jr., S. Gattaleeradhan, R. D. Farley, and C. C. Waits (2002), An examination of the convective charging hypothesis: Charge structure, electric fields, and Maxwell currents, *J. Geophys. Res.*, *107*(D22), 4630, doi:10.1029/2001JD001495.
- Hobbs, P. V., and A. L. Rangno (1985), Ice particle concentrations in clouds, *J. Atmos. Sci.*, *42*, 2523–2549.
- Jacobson, E. A., and E. P. Krider (1976), Electrostatic field changes produced by Florida lightning, *J. Atmos. Sci.*, *33*, 103–117.
- Jayarathne, E. R. (1993), The heat balance of a riming graupel pellet and the charge separation during ice-ice collisions, *J. Atmos. Sci.*, *50*(18), 3185–3193.
- Jayarathne, E. R. (1998), Density and surface temperature of graupel and the charge separation during ice crystal interactions, *J. Geophys. Res.*, *103*(D12), 13,957–13,961.
- Jayarathne, E. R., and C. P. R. Saunders (1985), Thunderstorm electrification: The effect of cloud droplets, *J. Geophys. Res.*, *90*(D7), 13,063–13,066.
- Jayarathne, E. R., C. P. R. Saunders, and J. Hallett (1983), Laboratory studies of the charging of soft hail during ice crystal interactions, *Q. J. R. Meteorol. Soc.*, *109*, 609–630.
- Jennings, S. G. (1975), Electric charging of water drops in polarizing electric fields, *J. Electrostat.*, *1*, 15–25.
- Jhavar, D. S., and J. A. Chalmers (1967), Point-discharge currents through small trees in artificial fields, *J. Atmos. Terr. Phys.*, *29*, 1459–1463.
- Kato, T. (1995), A box-Lagrangian rain-drop scheme, *J. Meteorol. Soc. Jpn.*, *73*(2), 241–245.
- Keith, W. D., and C. P. R. Saunders (1989), The collection efficiency of a cylindrical target for ice crystals, *Atmos. Res.*, *23*, 83–95.
- Keith, W. D., and C. P. R. Saunders (1990), Further laboratory studies of the charging of graupel during ice crystal interactions, *Atmos. Res.*, *25*, 445–464.
- Klemp, J. B., and R. B. Wilhelmson (1978), Simulations of right- and left-moving storms produced through storm splitting, *J. Atmos. Sci.*, *35*, 1097–1110.
- Krehbiel, P. R., R. Tennis, M. Brook, W. W. Holmes, and R. Comes (1984), A comparative study of the initial sequence of lightning in a small florida thunderstorm, in *Proceedings of 7th International Conference on Atmospheric Electricity*, pp. 279–285, Am. Meteorol. Soc., Boston, Mass.
- Krehbiel, P. R., W. R. Thomas, T. Hamlin, J. Harlin, M. Stanley, J. Lombardo, and D. Shown (2000), Inverted polarity lightning in STEPS, *Eos Trans. AGU*, *81*(48), Fall Meet. Suppl., Abstract A62D–06.
- Lang, T. J., et al. (2004), The Severe Thunderstorm Electrification and Precipitation Study, *Bull. Am. Meteorol. Soc.*, *85*(8), 1107–1125, doi:10.1175/BAMS-85-8-1107.
- Latham, J., and B. J. Mason (1962), Electrical charging of hail pellets in a polarizing electric field, *Proc. R. Soc. London, Ser. A*, *266*, 387–401.
- Leonard, B. P. (1991), The ULTIMATE conservative difference scheme applied to unsteady one-dimensional advection, *Comput. Methods Appl. Mech. Eng.*, *88*, 17–74.
- Lhermitte, R., and P. R. Krehbiel (1979), Doppler radar and radio observations of thunderstorms, *IEEE Trans. Geosci. Electron.*, *GE-17*(4), 162–171.
- Lhermitte, R. M., and E. R. Williams (1985), Thunderstorm electrification: A case study, *J. Geophys. Res.*, *90*, 6071–6078.
- MacGorman, D. R., and W. D. Rust (1998), *The Electrical Nature of Storms*, 422 pp., Oxford Univ. Press, New York.
- MacGorman, D. R., J. M. Straka, and C. L. Ziegler (2001), A lightning parameterization for numerical cloud models, *J. Appl. Meteorol.*, *40*, 459–478.
- Mansell, E. R., D. R. MacGorman, C. L. Ziegler, and J. M. Straka (2002), Simulated three-dimensional branched lightning in a numerical thunderstorm model, *J. Geophys. Res.*, *107*(D9), 4075, doi:10.1029/2000JD000244.
- Marshall, B. J. P., J. Latham, and C. P. R. Saunders (1978), A laboratory study of charge transfer accompanying collision of ice crystals with a simulated hailstone, *Q. J. R. Meteorol. Soc.*, *104*, 163–178.
- Marshall, T. C., M. P. McCarthy, and W. D. Rust (1995), Electric field magnitudes and lightning initiation in thunderstorms, *J. Geophys. Res.*, *100*(D4), 7097–7103.
- Mason, B. J. (1971), *The Physics of Clouds*, 670 pp., Clarendon, Oxford, U. K.
- Mason, B. J. (1988), The generation of electric charges and fields in thunderstorms, *Proc. R. Soc. London, Ser. A*, *415*, 303–315.
- Meyers, M. P., P. J. DeMott, and W. R. Cotton (1992), New primary ice-nucleation parameterizations in an explicit cloud model, *J. Appl. Meteorol.*, *31*, 708–721.
- Moeng, C.-H. (1984), A large-eddy-simulation model for the study of planetary boundary-layer turbulence, *J. Atmos. Sci.*, *41*, 2052–2062.
- Pasko, V. P., M. A. Stanley, J. D. Mathews, U. S. Inan, and T. G. Wood (2002), Electrical discharge from a thundercloud top to the lower ionosphere, *Nature*, *416*, 152–154.
- Pereyra, R. G., E. E. Avila, N. E. Castellano, and C. Saunders (2000), A laboratory study of graupel charging, *J. Geophys. Res.*, *105*(D16), 20,803–20,812.
- Randell, S. C., S. A. Rutledge, R. D. Farley, and J. H. Helsdon Jr. (1994), A modeling study of the early electrical development of tropical convection: Continental and oceanic (monsoon) storms, *Mon. Weather Rev.*, *122*, 1852–1877.
- Rawlins, F. (1982), A numerical study of thunderstorm electrification using a three dimensional model incorporating the ice phase, *Q. J. R. Meteorol. Soc.*, *108*, 779–800.
- Reynolds, S. E., M. Brook, and M. F. Gourley (1957), Thunderstorm charge separation, *J. Meteorol.*, *14*, 426–436.
- Rison, W., R. J. Thomas, P. R. Krehbiel, T. Hamlin, and J. Harlin (1999), A GPS-based three-dimensional lightning mapping system: Initial observations in central New Mexico, *Geophys. Res. Lett.*, *26*, 3573–3576.
- Rosenfeld, D., and W. L. Woodley (2000), Deep convective clouds with sustained supercooled liquid water down to -37.5°C , *Nature*, *405*, 440–441.
- Rust, W. D., and D. R. MacGorman (2002), Possibly inverted-polarity electrical structures in thunderstorms during STEPS, *Geophys. Res. Lett.*, *29*(12), 1571, doi:10.1029/2001GL014303.
- Sartor, J. D. (1981), Induction charging of clouds, *J. Atmos. Sci.*, *38*, 218–220.
- Saunders, C. P. R., and I. M. Brooks (1992), The effects of high liquid water on thunderstorm charging, *J. Geophys. Res.*, *97*, 14,671–14,676.
- Saunders, C. P. R., and S. L. Peck (1998), Laboratory studies of the influence of the rime accretion rate on charge transfer during crystal/graupel collisions, *J. Geophys. Res.*, *103*, 13,949–13,956.
- Saunders, C. P. R., W. D. Keith, and R. P. Mitzewa (1991), The effect of liquid water on thunderstorm charging, *J. Geophys. Res.*, *96*, 11,007–11,017.
- Saunders, C. P. R., E. E. Avila, S. L. Peck, N. E. Castellano, and G. G. A. Varela (1999), Vapor and heat supply to riming graupel: Effect on charging, paper presented at 11th International Conference on Atmospheric Electricity, Guntersville, Ala.
- Scavuzzo, C. M., and G. M. Caranti (1996), Thunderstorm electrification analysis: The dependence on the temperature-LWC diagram, *J. Atmos. Sci.*, *53*, 349–358.
- Scavuzzo, C. M., S. Masuelli, G. M. Caranti, and E. R. Williams (1998), A numerical study of thundercloud electrification by graupel-crystal collisions, *J. Geophys. Res.*, *103*, 13,963–13,973.
- Shreve, E. L. (1970), Theoretical derivation of atmospheric ion concentrations, conductivity, space charge density, electric field and generation rate from 0 to 60 km, *J. Atmos. Sci.*, *27*, 1186–1194.
- Simpson, G. C., and F. J. Scrase (1937), The distribution of electricity in thunderclouds, *Proc. R. Soc. London, Ser. A*, *161*, 309–352.
- Solomon, R., and M. B. Baker (1998), Lightning flash rate and type in convective storms, *J. Geophys. Res.*, *103*(D12), 14,041–14,057.
- Standler, R. B., and W. P. Winn (1979), Effects of coronae on electric fields beneath thunderstorms, *Q. J. R. Meteorol. Soc.*, *105*, 285–302.
- Straka, J. M. (1989), Hail growth in a highly glaciated central High Plains multi-cellular hailstorm, Ph.D. thesis, Univ. of Wis., Madison.
- Straka, J. M., and J. R. Anderson (1993a), Numerical simulations of microburst-producing storms: Some results from storms observed during COHMEX, *J. Atmos. Sci.*, *50*, 1329–1348.
- Straka, J. M., and J. R. Anderson (1993b), Extension and application of a local, minimum aliasing method to multidimensional problems in limited-area domains, *Mon. Weather Rev.*, *121*, 2903–2918.
- Straka, J. M., and E. R. Mansell (2005), A bulk microphysics parameterization with multiple ice precipitation categories, *J. Appl. Meteorol.*, *44*, 445–466.
- Takahashi, T. (1978), Riming electrification as a charge generation mechanism in thunderstorms, *J. Atmos. Sci.*, *35*, 1536–1548.
- Takahashi, T. (1979), Warm cloud electricity in a shallow axisymmetric cloud model, *J. Atmos. Sci.*, *36*, 2236–2258.

- Takahashi, T. (1984), Thunderstorm electrification – A numerical study, *J. Atmos. Sci.*, *41*, 2541–2558.
- Takahashi, T., and K. Miyawaki (2002), Reexamination of riming electrification in a wind tunnel, *J. Atmos. Sci.*, *59*(5), 1018–1025.
- Tremback, C. J., J. Powell, W. R. Cotton, and R. A. Pielke (1987), The forward-in-time upstream advection scheme: Extension to higher orders, *Mon. Weather Rev.*, *115*, 540–555.
- Ushio, T., S. Heckman, H. Christian, and Z.-I. Kawasaki (2003), Vertical development of lightning activity observed by the LDAR system—Lightning bubbles, *J. Appl. Meteorol.*, *42*, 165–174.
- Vonnegut, B. (1953), Possible mechanism for the formation of thunderstorm electricity, *Bull. Am. Meteorol. Soc.*, *34*, 378.
- Weisman, M. L., and J. B. Klemp (1982), The dependence of numerically simulated convective storms on vertical wind shear and buoyancy, *Mon. Weather Rev.*, *110*, 504–520.
- Weisman, M. L., and J. B. Klemp (1984), The structure and classification of numerically simulated convective storms in directionally varying wind shears, *Mon. Weather Rev.*, *112*, 2479–2498.
- Whipple, F. J. W., and J. A. Chalmers (1944), On Wilson's theory of the collection of charge by falling drops, *Q. J. R. Meteorol. Soc.*, *70*, 103–118.
- Williams, E., and R. Zhang (1996), Density of rime in laboratory simulations of thunderstorm microphysics and electrification, *J. Geophys. Res.*, *101*(D23), 29,715–29,719.
- Williams, E. R. (1989), The triple structure of thunderstorms, *J. Geophys. Res.*, *94*, 13,151–13,167.
- Williams, E. R., M. E. Weber, and R. E. Orville (1989), The relationship between lightning type and convective state of thunderclouds, *J. Geophys. Res.*, *94*(13), 213–220.
- Williams, E. R., R. Zhang, and J. Rydock (1991), Mixed-phase microphysics and cloud electrification, *J. Atmos. Sci.*, *48*(19), 2195–2203.
- Workman, E. J., and S. E. Reynolds (1949), Electrical activity as related to thunderstorm cell growth, *Bull. Am. Meteorol. Soc.*, *30*, 142–144.
- Ziegler, C. L. (1985), Retrieval of thermal and microphysical variables in observed convective storms. Part I: Model development and preliminary testing, *J. Atmos. Sci.*, *42*, 1487–1509.
- Ziegler, C. L., and D. R. MacGorman (1994), Observed lightning morphology relative to modeled space charge and electric field distributions in a tornadic storm, *J. Atmos. Sci.*, *51*, 833–851.
- Ziegler, C. L., P. S. Ray, and D. R. MacGorman (1986), Relations of kinematics, microphysics and electrification in an isolated mountain thunderstorm, *J. Atmos. Sci.*, *43*, 2098–2114.
- Ziegler, C. L., D. R. MacGorman, J. E. Dye, and P. S. Ray (1991), A model evaluation of non-inductive graupel-ice charging in the early electrification of a mountain thunderstorm, *J. Geophys. Res.*, *96*(D7), 12,833–12,855.

D. R. MacGorman, E. R. Mansell, and C. L. Ziegler, National Severe Storms Laboratory, 1313 Halley Circle, Norman, OK 73069, USA. (mansell@ou.edu; web: <http://www.cimms.ou.edu/~mansell>)

J. M. Straka, School of Meteorology, University of Oklahoma, Norman, OK 73069, USA.